Electromagnetic Wave Transmission through Sub-wavelength Channels and Bends Using Metallic Wires

by

Mani Kashanianfard

A thesis
presented to the University of Waterloo
in fulfillment of the
thesis requirement for the degree of
Master of Applied Science
in
Electrical and Computer Engineering

Waterloo, Ontario, Canada, 2009

I hereby declare that I am the sole author of this thesis. This is a true copy of the thesis, including any required final revisions, as accepted by my examiners.

I understand that my thesis may be made electronically available to the public.

Abstract

Techniques and technologies to transfer electromagnetic energy through sub-wavelength channels have been researched extensively in the past few years because their application in different areas such as sub-wavelength imaging, telecommunication, increasing the storage capacity, and confinement and transmission of electromagnetic energy. Common ways of achieving such transmission includes exciting surface plasmon polaritons on both sides of the cannel or using double negative metamaterials.

Recently a mechanism to squeeze the electromagnetic energy through sub-wavelength channels using materials with extremely small permittivity was introduced. Such materials may be found naturally at some limited frequencies in the infrared and optical frequency ranges, but they are commonly fabricated for a desired frequency as engineered metamaterials by by embedding metallic inclusions in a dielectric medium. The main problem with the engineered materials is that they have relatively large losses at their low permittivity frequency.

In this thesis,I have presented a novel structure consisting of arrays of metallic wires that can be used to squeeze electromagnetic energy through sub-wavelength channels and junctions with negligible loss. The theory of transmission through such array is derived and design methods to tune the transmission frequency is provided. The structure is also tested numerically and experimentally in several geometries and results are compared with previous methods.

Acknowledgements

I would like to thank all the people who made this possible.

Dedication

This is dedicated to my parents.

Contents

List of Tables

List of Figures

Chapter 1

Introduction

In recent years, several techniques to transfer electromagnetic energy through sub-wavelength structures have been introduced[5, 6, 7, 8]. These transmissions are of interest for various application including sub-wavelength imaging[9, 10], increasing the storage capacity[11], and confinement and transmission of electromagnetic energy [12, 13]. Transmission through sub-wavelength structures can also be achieved using materials with extremely small permittivity (epsilon near zero materials)[1]. It is shown that electromagnetic energy can be squeezed and transmitted trough narrow waveguide channels and bends if filled by epsilon near zero(ENZ) materials[2]. Such materials may be found naturally at some limited frequencies in the infrared and optical frequency ranges or may be synthesized as metamaterials at the desired frequency by embedding inclusions in a dielectric medium[3]. The main advantage of using the inclusions as ENZ materials over the other techniques of tunneling energy is that the transmission frequency is independent of the shape of the junction or bend and is only related to the plasma frequency of the ENZ materials. However, the inclusions are highly resonant in their plasma frequency where ENZ behavior dominates. These resonances produce highly concentrated electromagnetic fields and currents, thus increasing the effect of both metallic and dielectric losses[3]. An alternative method of realizing the ENZ behavior is to use a waveguide at its cutoff frequency[4, 14]. It can be verified that any waveguide behaves as ENZ near its cutoff frequency, however, the cutof frequency cannot be selected independent of the geometry of the waveguide. In other words, the cutoff frequency is determined by the width of the waveguide and may not be the desired frequency of operation. Furthermore, squeezing energy using the waveguide cutoff method has inherently smaller bandwidth and cannot be used if the waveguides do not have a dielectric filling[4, 14].

In this thesis, we propose a novel structure consisting of metallic wires that can be used to squeeze and transmit electromagnetic field trough narrow channels and waveguide bends of arbitrary angles. The frequency of transmission can be tuned as desired independently of

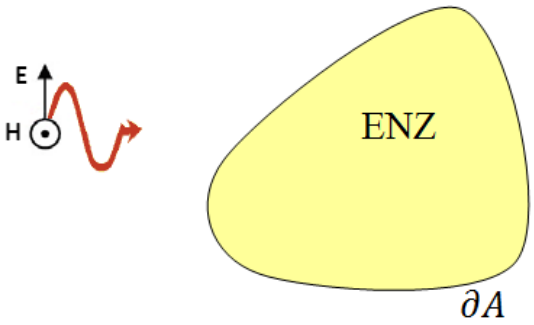

Figure 1.1: Scattering from a 2D cylinder of ENZ material.

the dimensions of the waveguides. The wires structure proposed here allows for reduction of metallic and dielectric losses since the wires are much thicker than metamaterial inclusions operating at the same frequency and there is no use of any dielectric to mechanically support the wires.

1.1 Background

In this section we will present the fundamentals of tunneling with ENZ materials and study the important characteristics of such transmission.

1.1.1 Theory of tunneling EM waves through ENZ materials

We begin with the problem of scattering of time harmonic electromagnetic waves from a two dimensional (z-invariant) cylinder of arbitrary cross-section as shown in Fig.1.1 [1]. Assume a plane wave excitation with magnetic field of $\mathbf{H}^{inc} = \psi^{inc}\hat{\mathbf{u}}_z$. The total magnetic field (incident and scattered) can be expressed as $\mathbf{H} = H_z\hat{\mathbf{u}}_z$ provided that the geometry and incident field are z-invariant. The total electric field is then found to be:

$$\mathbf{E} = \frac{1}{j\omega\epsilon}\nabla H_z \times \hat{\mathbf{u}}_z \tag{1.1}$$

If we assume that ϵ is zero at the working frequency, 1.1 suggests that ∇H_z has to be zero inside the ENZ cylinder since the electric field cannot be infinite. This means that the magnetic field has to be constant inside the ENZ. Namely, $H_z = H_z^{int}$. The magnetic field outside the ENZ medium is not constant and is given by the solution of

$$\nabla \cdot (\frac{1}{\epsilon^{ext}}\nabla H_z) + \omega^2\mu H_z = 0, \tag{1.2}$$

subject to the boundary condition $H_z = H_z^{int}$ over the boundary of ENZ cylinder. Using the superposition principle, the magnetic field outside ENZ medium can be expressed as the summation of tow parts: solution to the problem of zero excitation and constant magnetic field of H_z^{int} on the ENZ boundary and solution to the problem of plane wave excitation and zero magnetic field on the boundary of ENZ (i.e. replacing ENZ with perfect magnetic conductor). The total magnetic field is the addition of these two solutions:

$$H_z = \psi^{PMC} + H_z^{int}\psi_1^s \tag{1.3}$$

Here ψ^{PMC} is the solution with the same excitation and with ENZ replaced with a perfect magnetic conductor(PMC). ψ_1^s is the solution for the exterior problem with no excitation and boundary condition of $\psi_1^s = 1$ on the boundary of ENZ and sommerfeld's radiation conditions at infinity. In order to determine the unknown H_z^{int}, we use Faraday's law to calculate electromotive force around the boundary of ENZ medium(∂A):

$$\oint_{\partial A} \mathbf{E}\cdot\mathbf{dl} = -j\omega\mu_0\mu_{r,p}H_z^{int}A_p \tag{1.4}$$

where $\mu_{r,p}$ is the relative permeability of the cylinder and A_p is its cross-sectional area. The term $\mathbf{E}\cdot\mathbf{dl}$ can be written as $E_t dl$ where E_t is the tangential component of the electric field. Since E_t has to be continues on the boundary we can use 1.3 and 1.1 (with ϵ changed to ϵ^{ext}) to find E_t:

$$E_t = (\hat{\mathbf{u}}_z \times \hat{\mathbf{n}})\cdot\mathbf{E} = -\frac{1}{j\omega\epsilon^{ext}}\hat{\mathbf{n}}\cdot\nabla H_z = -\frac{1}{j\omega\epsilon_0\epsilon_r^{ext}}\frac{\partial}{\partial n}H_z \tag{1.5}$$

therefore the left hand side of 1.4 becomes:

$$\oint_{\partial A} \mathbf{E}\cdot\mathbf{dl} = -\frac{1}{j\omega\epsilon_0}\left(\oint_{\partial A}\frac{1}{\epsilon_r^{ext}}\frac{\partial\psi^{PMC}}{\partial n}dl + H_z^{int}\oint_{\partial A}\frac{1}{\epsilon_r^{ext}}\frac{\partial\psi_1^s}{\partial n}dl\right) \tag{1.6}$$

where $\hat{\mathbf{n}}$ is the outward unit vector normal to ∂A. Substituting 1.6 in 1.4 will give the sublation for H_z^{int}:

$$H_z^{int} = \frac{-\oint_{\partial A}\frac{1}{\epsilon_r^{ext}}\frac{\partial\psi^{PMC}}{\partial n}dl}{\oint_{\partial A}\frac{1}{\epsilon_r^{ext}}\frac{\partial\psi_1^s}{\partial n}dl + k_0^2\mu_{r,p}A_p} \tag{1.7}$$

where $k_0 = \omega\sqrt{\epsilon_0\mu_0}$ is the wave number in free space.

We can now use this results to derive a formula for the reflection coefficient of the general waveguide geometry of Fig.1.2.[1] The geometry consists of two parallel plate waveguides with thicknesses of a_1 and a_2 that are connected to each other via an ENZ section. The geometry of the ENZ section can be selected arbitrarily. The only assumption on this geometry is that the two faces that connect the ENZ section to the waveguides are perpendicular to the walls of the waveguides. All the other faces of the ENZ section are covered

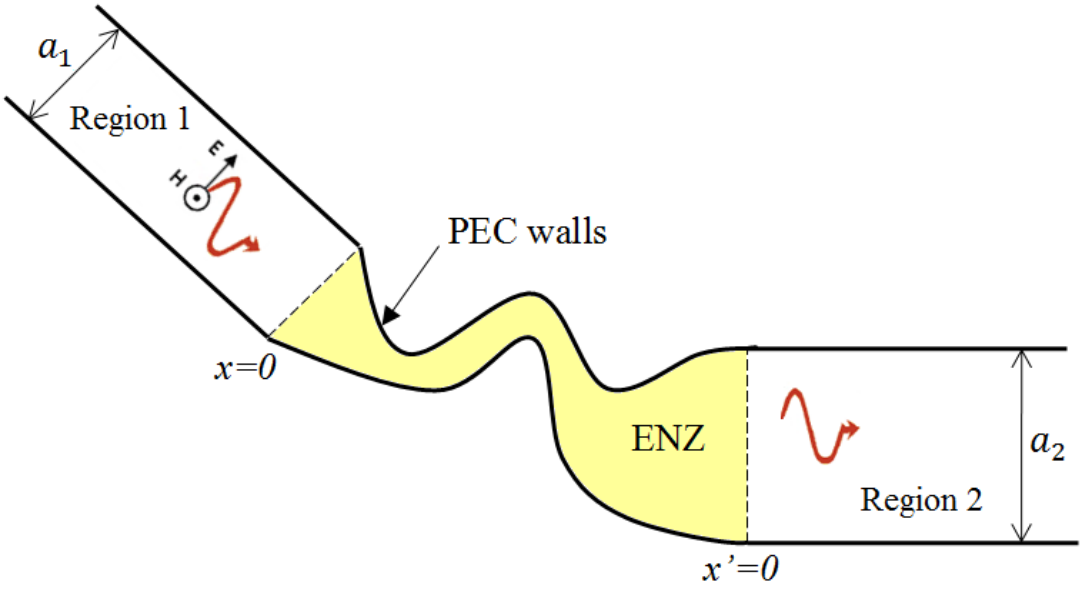

Figure 1.2: Geometry of a 2D waveguide structure with an ENZ material section.

with perfect electric conductor(PEC) walls. We assume that the parallel plate waveguides are filled with air and the transverse electromagnetic (TEM) mode of the left hand side waveguide is excited. The magnetic field of this mode is given by $H_z = \psi^{inc} = H_z^{inc} e^{-jk_0 x}$, which is in the form of a plane wave. Therefore the above derivation can be used here. It is straightforward to find ψ^{PMC} and ψ_1^s for this geometry:

$$\begin{array}{lllll} \text{in region1:} & \psi^{PMC} = H_z^{inc}\left(e^{-jk_0 x} - e^{jk_0 x}\right) & \text{and} & \psi_1^s = e^{jk_0 x} \\ \text{in region2:} & \psi^{PMC} = 0 & \text{and} & \psi_1^s = e^{-jk_0 x\prime} \end{array} \tag{1.8}$$

Note that the origin of the unprimed coordinates is at the left interface and the origin of the primed coordinates is at the right interface. Using 1.3 the total magnetic field in region1 can be written as $H_z = H_z^{inc} e^{-jk_0 x} + (H_z^{int} - H_z^{inc}) e^{jk_0 x}$, which means the reflection coefficient can be found as $\rho = H_z^{int}/H_z^{inc} - 1$. The ratio H_z^{int}/H_z^{inc} is found by substituting 1.8 in 1.7. The reflection coefficient is the given by:

$$\rho = \frac{(a_1 - a_2) - jk_0\mu_{r,p}A_p}{(a_1 + a_2) + jk_0\mu_{r,p}A_p} \tag{1.9}$$

$\rho = \frac{H_z^{int}}{H_z^{inc}} - 1$ and:

$$|\rho|^2 = \left(\frac{a_1 - a_2}{a_1 + a_2}\right)^2 + \frac{4a_1 a_2}{(a_1 + a_2)^2}\left(\frac{(k_0\mu_{r,p}A_p)^2}{(a_1 + a_2)^2 + (k_0\mu_{r,p}A_p)^2}\right) \tag{1.10}$$

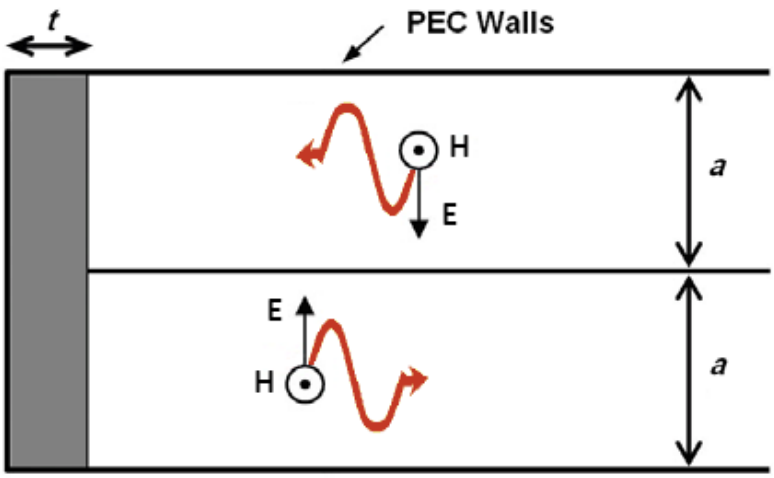

Figure 1.3: Geometry of a 180° bend in a parallel plate waveguide. The shaded area is filled with ENZ material

The magnitude of the reflection coefficient is always bigger than or equal to $|a_1 - a_2|/(a_1 + a_2)$, which means in order to have zero reflection, the thicknesses of the two waveguides have to be equal. Considering $a_1 = a_2 = a$, in order for reflection coefficient to be very small, the condition $k_0\mu_{r,p}A_p/2a \ll 1$ must be satisfied. This leads to a very interesting conclusion that the wave is fully transmitted through the ENZ channel if its cross-sectional area A_p is electrically small. Note that for a fixed a, it is always possible to design the shape of ENZ channel so that $k_0A_p/2a$ is arbitrarily small by decreasing its width.

1.1.2 Numerical verification of tunneling in different geometries

One possible way to realize a narrow ENZ channel with perpendicular faces to waveguide walls is the geometry of Fig.1.3[1]. The structure consist of two parallel plate waveguides parallel to each other and forming a 180° bend. Based on the discussion in previous chapter, if the thickness t of the ENZ material is small compared to the wavelength, we expect full transmission from one waveguide to another. This particular geometry has been analyzed in [1] the results are presented in this section. Assume that the bend is filled with a Drude-type dispersion model with permittivity of

$$\epsilon = \epsilon_0(1 - \frac{\omega_p^2}{\omega(\omega + j\Gamma)}), \tag{1.11}$$

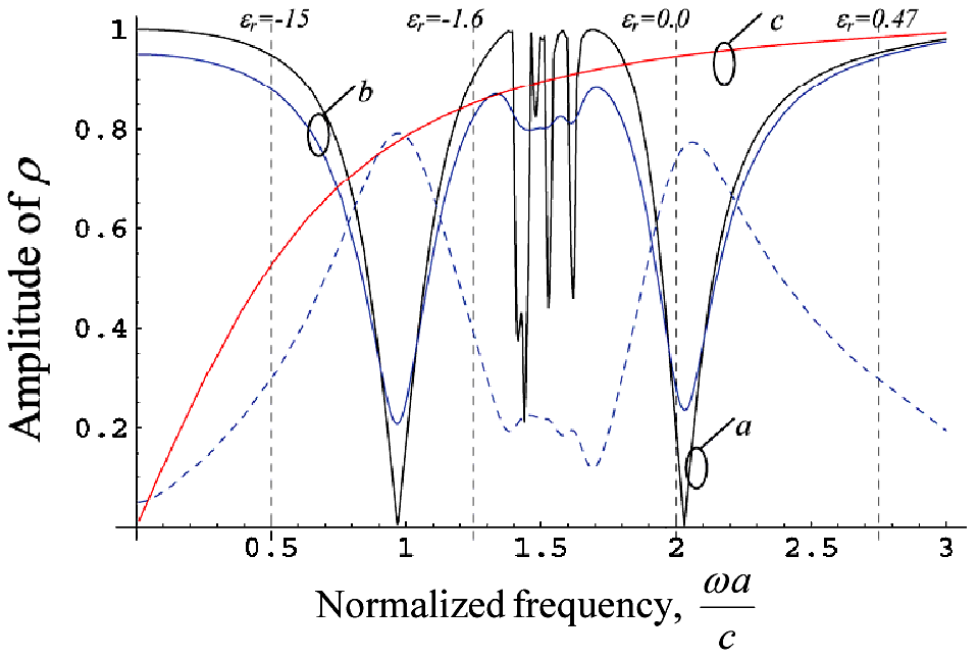

Figure 1.4: Reflection coefficient as a function of normalized frequency. Curve a: $\Gamma = 0$, Curve b: $\Gamma/\omega_p = 0.05$, Curve c: without ENZ. The dashed curve represents the transmission coefficient for $\Gamma/\omega_p = 0.05$.(the graph is taken from [1])

where ω_p is the plasma frequency and Γ is the collision frequency. The thickness of the ENZ layer is $t = 0.1a$ and ω_p is chosen so that $\omega_p a/c = 2.0$. The amplitude of the reflection coefficient is calculated using the commercial software CST Microwave Studio for the lossless case($\Gamma = 0$) and for $\Gamma/\omega_p = 0.05$. The result is shown in Fig.1.4[1]. As predicted by the theory, the reflection coefficient is 0.2 when ϵ is exactly equal to zero. Note that the actual full transmission accurse at a frequency where ϵ is slightly higher than zero. For the more realistic case of $\Gamma/\omega_p = 0.05$, full tunneling is not possible and the reflection coefficient never reaches zero. In addition to the part of the energy that is reflected, a non-negligible portion of the energy will be wasted (converted to heat) because of the losses in ENZ media. The dashed line in Fig.1.4 shows the transmission coefficient for $\Gamma/\omega_p = 0.05$. If we look at the frequency ω_p $(2a/c)$, the reflected energy is less than 10% but the transmitted energy is only about 60% which means about 30% of the initial energy is wasted. The reflection coefficient for the bend without ENZ is also shown in Fig.1.4 for comparison. There is no transmission possible when the ENZ is removed (except for the static limit).

Another interesting geometry that has been used to show the coupling properties of ENZ[2] is shown in Fig.1.5. The geometry consists of two parallel plate waveguides that

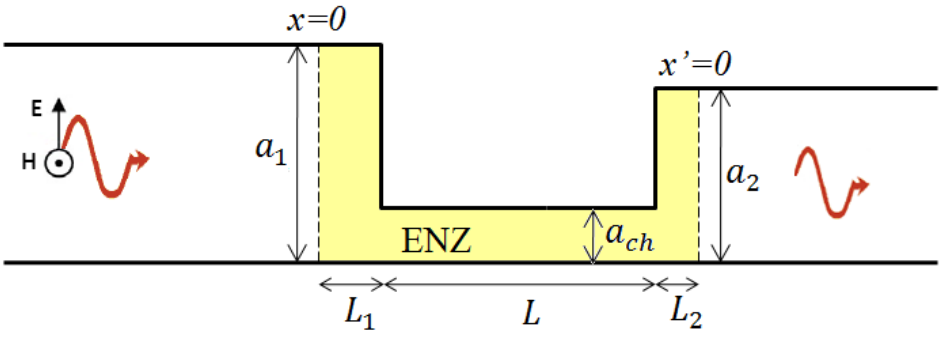

Figure 1.5: Geometry of two parallel plate waveguides connected to each other via a U-shaped narrow channel. The shaded area is filled with ENZ material.

are connected to each other via a U-shaped narrow channel. The channel is filled with ENZ material. The total area of the x-y plane cross-section of the ENZ material can be calculated as $A_p = L_1a_1 + L_2a_2 + La_{ch}$. If $a_1 = a_2 = a$ and we assume that L_1,L_2 and a_{ch} are electrically small, A_p satisfies the requirement derived in the starting section of this chapter (i.e. $k_0\mu_{r,p}A_p/2a \ll 1$). Therefore, we can expect full transition at the plasma frequency of the ENZ material.

Fig.1.6 shows the results of numerical analysis of the case using CST Microwave Stodio[2]. The dimensions are: $L_1 = L_2 = a_{ch} = 0.1a$ and $L = a$, and the permittivity ϵ of the ENZ material is the same as before ($\epsilon = \epsilon_0(1 - \omega_p^2/\omega(\omega + j\Gamma))$). As seen in the graph, the energy is almost fully transmitted in the low-loss case($\Gamma = 0.001\omega_p$). In the lossy case, full transmission is not possible but a large portion of the energy is still transmitted when the loss is moderate.

The transmission coefficient in absence of ENZ material is also plotted in Fig.1.6. It is shown that when ENZ is removed no transmission is possible at the plasma frequency ω_p, therefore ENZ in fact enhanced the transmission. However, it is seen that the field is fully transmitted at a frequency higher than ω_p even without the ENZ material. This transmission is related to the resonances of the geometry of the U-shaped channel(Fabry-Parot-type transmission). The frequency of this transmission depends on the values of L,a and a_{ch} and cannot be tuned independent of the geometry of the waveguide.

The last geometry that we study here is shown in Fig.1.7. This geometry consists of two parallel plate waveguides connected to each other via a 90° bend that is filled with ENZ material. The same material as before ($\epsilon = \epsilon_0(1 - \omega_p^2/\omega(\omega + j\Gamma))$) is used here and the thickness of ENZ section is again $0.1a$ ($a_{imp} = 0.9a$). Fig.1.7 also shows the real part of Poynting vector at the plasma frequency. It is shown that the Poynting vector lines are bent traveled through the ENZ material.

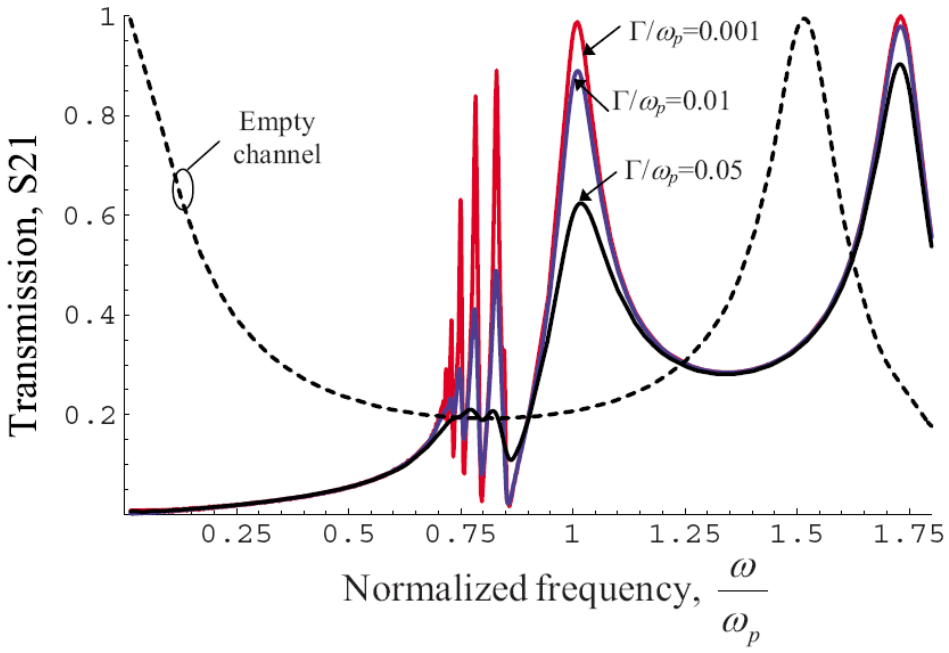

Figure 1.6: Transmission coefficient for the U-shaped Narrow channel with different loss factors. The dashed line shows transmission coefficient of the same geometry without ENZ.(the graph is taken from [2])

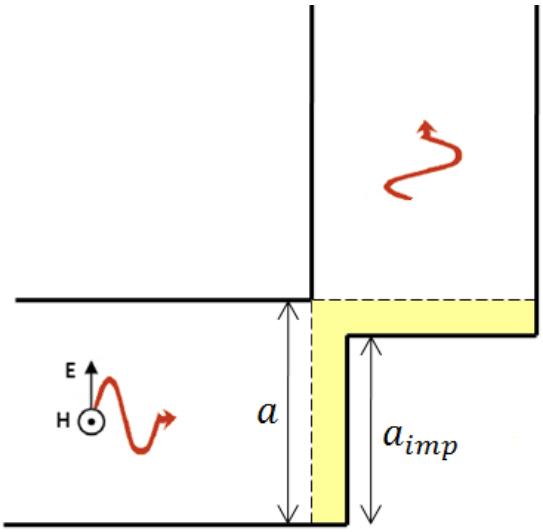

Figure 1.7: Geometry of the 90° bent parallel plate waveguide and real part of the Poynting vector at plasma frequency.

The transmission coefficient of the 90° bent waveguide geometry is given in Fig.1.8 for a range of frequencies. Similar to other geometries that we discussed, there is a significant improvement in the transmission coefficient when ENZ is inserted compared to the case in which the bend is filled with air(dashed curve in Fig.1.8)

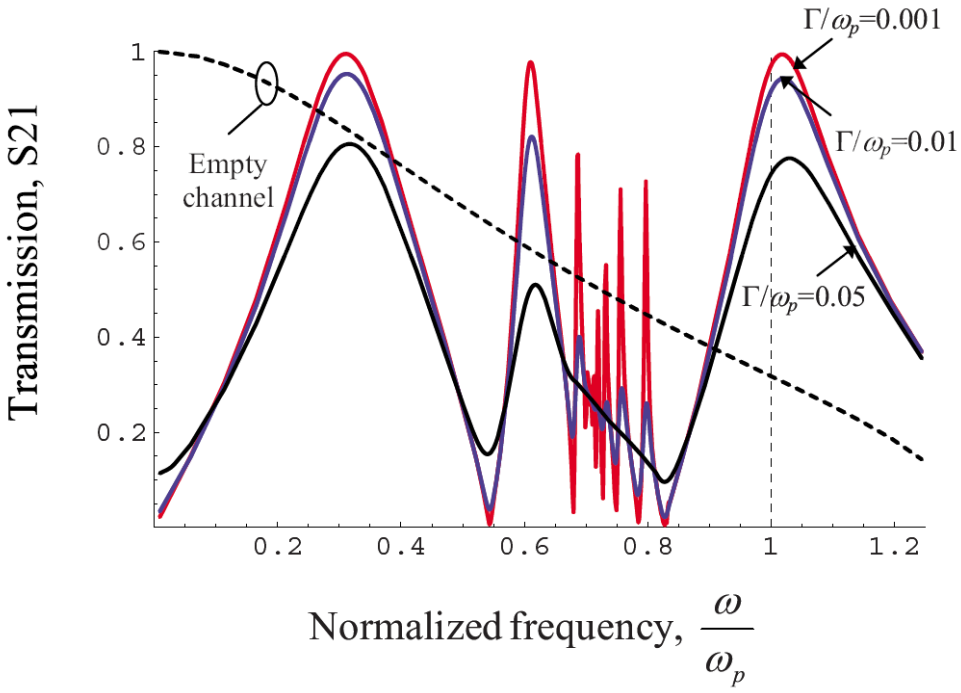

Figure 1.8: Transmission coefficient for the U-shaped Narrow channel with different loss factors. The dashed line shows transmission coefficient of the same geometry without ENZ.(the graph is taken from [1])

1.1.3 Experimental verification of tunneling in ENZ materials

An experimental demonstration of tunneling using ENZ materials was presented in [3]. The ENZ medium was realized by patterning complementary split ring resonators(CSRR)[15] in one of the ground planes of the narrow channel shown in Fig.1.5. To validate the tunneling effect, the scattering parameters of a channel patterned with CSRR was compared with that of an empty channel. In the experiment, the thickness of the channel and the thickness of the waveguides a was chosen to be 1mm and 11mm respectively. The structure was also analytically modeled using the approximate expressions for permittivity of CSRR. The experimental and theoretical results as well as the simulation results by the commercial software Ansoft HFSS is presented in Fig.1.9. Both simulation and experimental results show a relatively large loss (around 4dB) at the transmission frequency. The loss is due to the resonant behavior of the split ring resonators that creates a very large electric field in the dielectric medium in the channel and a very large electric current on the split ring resonators.

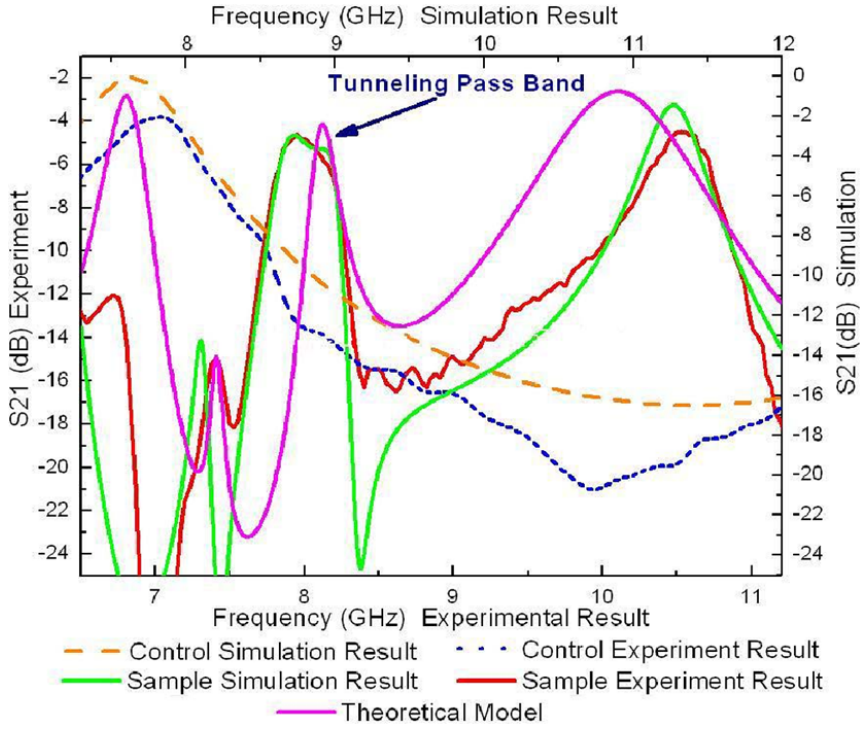

Figure 1.9: Experimental, simulation and theoretical derivation of the scattering parameters for the tunneling and control samples.(the graph is taken from[3])

1.1.4 Waveguide in cutoff as ENZ

Transverse electric (TE) modes of rectangular waveguides in the cut-off are known to have a dispersion relation similar to that of materials with negative permittivity[16, 17, 18]. The propagation constant of the TE^10 mode of a rectangular waveguide can be described as $\beta = \sqrt{((2\pi nf/c)^2 - (\pi/w)^2)}$[4], where n is the relative refractive index of the dielectric filling of the waveguide, w is the H-plane width of the waveguide, c is speed of light in vacuum and f is the frequency. This dispersion relation is similar to that of a plane wave traveling in a bulk material with the effective permittivity of:

$$\frac{\epsilon_{eff}}{\epsilon_0} = n^2 - \left(\frac{c^2}{4w^2}\right)\frac{1}{f^2} \tag{1.12}$$

The effective permeability μ_{eff} for this mode remains the same(μ_0). For frequencies close to cut-off ($f \approx c/2nw$), ϵ_{eff} is close to zero and the waveguide behaves effectively like ENZ materials.

The dispersion property of waveguides have been used to demonstrate the tunneling effect that was introduced in the beginning of this chapter[4, 14]. Fig.1.10 shows a schematic of the experimental setup that was used[4]. The setup consists of two rectangular waveguides of width $w = 102mm$ and height $h = 56mm$ that are filled with Teflon ($n = 1.41$), and an empty waveguide of the same width that connects the Teflon filled waveguides. The empty waveguide forms a very narrow U-shaped junction ($L_1 = L_2 = a_{ch} \ll h$) and has a cut-off frequency of $f_0 = 1.47GHz$. The Teflon filled waveguides are not in cut-off and support a propagating TE_{10} mode at this frequency. Following the above discussion and the results in section 1.1.2, we expect to see tunneling at frequencies around $1.47GHz$.

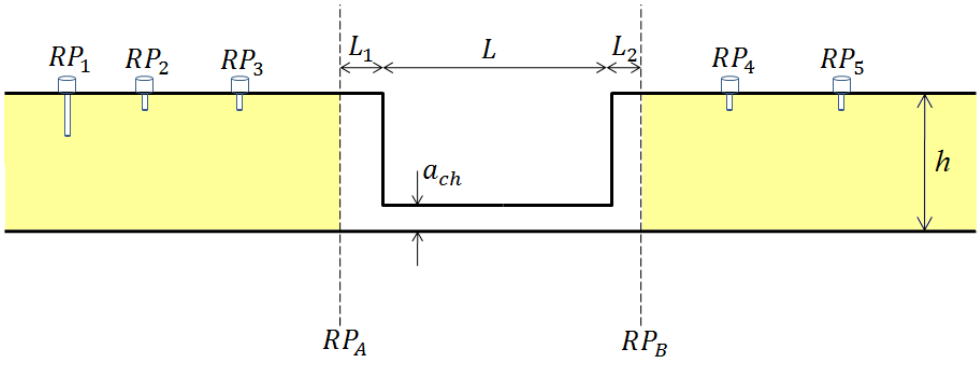

Figure 1.10: Experimental setup for verification of tunneling in a narrow waveguide channel

As shown in Fig.1.10, five probes are used to measure phase and amplitude of reflection and propagation coefficient in this setup. Probe RP_1 excites the TE_{10} mode of propagation

in the waveguide. RP_2 and RP_3 measure the phase and amplitude of electromagnetic waves in two different positions in the left hand side waveguide. The measured phase and amplitude can be used to decompose the field to its forward and backward traveling components referenced to the RP_A plane. The same procedure is applied to the left hand side waveguide using the data of probes RP_2 and RP_3 providing the forward and backward traveling waves referenced to RP_B plane. These four amplitudes have been used to find the complex reflection Γ and transmission T coefficients. The phase reference is selected so that $arg(T) = 0$ indicates a zero phase shift between RP_A and RP_B. Fig.1.11 shows the results for junctions of different lengthes. As predicted by the theory, there is a transmission band around the cut-off frequency. Note that changing the length of the channel only changes the bandwidth of transmission and the transmission frequency stays the same. Simulation results using CST Microwave Studio are also provided for comparison[4].

1.2 Thesis Organization

This thesis is organized as follows:

Chapter 2 introduces the proposed metallic wire structure. Electromagnetic wave transmission will be verified using numerical simulation and properties of this transmission will be discussed. In addition to simulation results, a theoretical study of the structure will be presented. A formula for calculating the transmission frequency will be given and the results will be compared with simulations.

Chapter 3 discusses the properties of transmission in wires in different 2D and 3D geometries. Design methods for tuning the transmission frequency regardless of the shape and size of the sub-wavelength channel is provided and the effect of changes in different parameters of the structure will be discussed. The simulation results of the 3D waveguide bend that we have fabricated is also presented.

Finally, a summary of the thesis and possible future research topics will be given in Chapter 4.

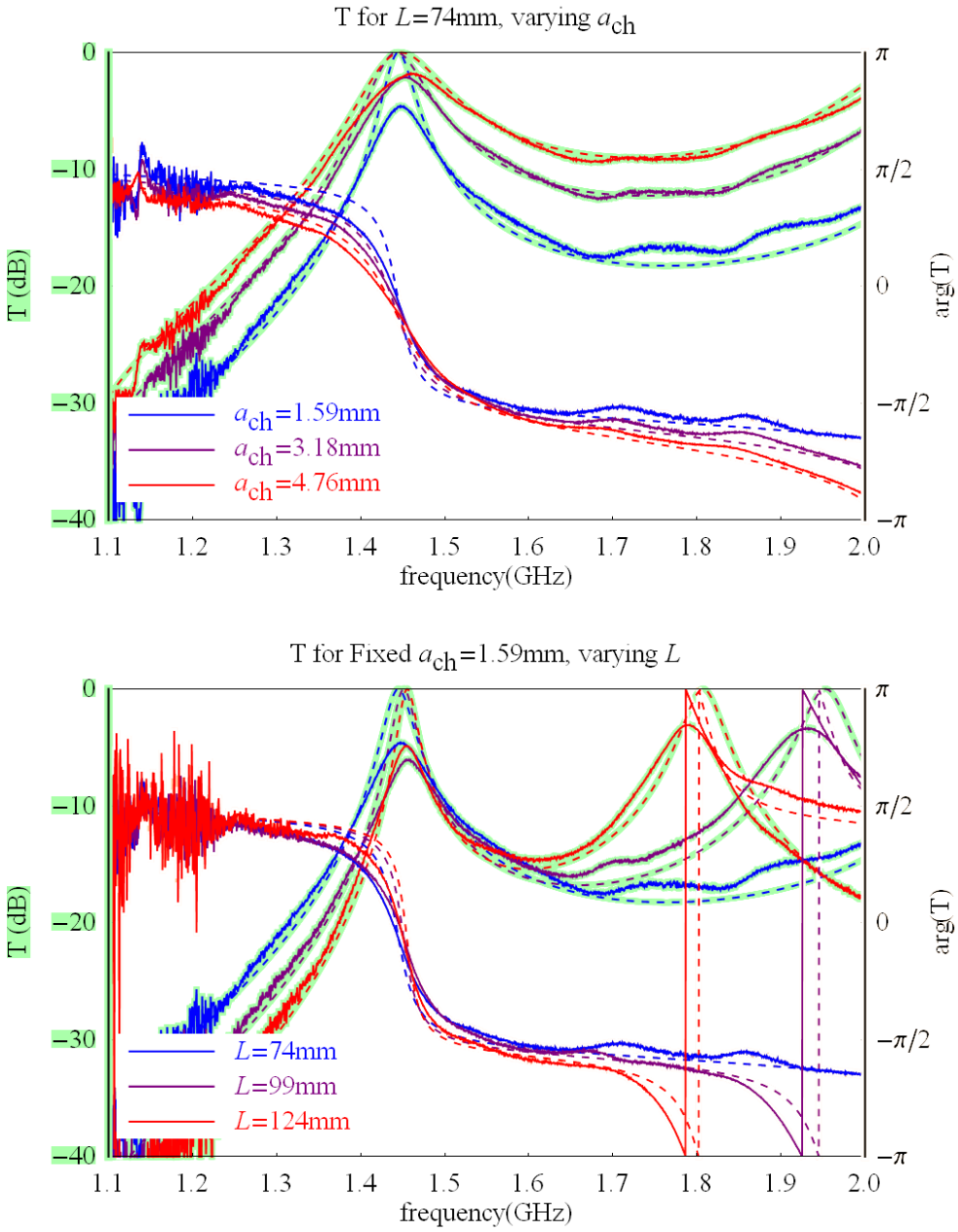

Figure 1.11: Experimental and simulation results for transmission through the U shaped junction for a fixed channel height of $a_ch = 1.59mm$ and different channel lengthes.(the graph is taken from [4])

Chapter 2

Metallic Wire Structure

In EMI/EMC applications, vias between adjacent layers of printed circuit boards provide strong electromagnetic coupling between the layers, which is often unwanted as it increases noise and cross-talk between different elements. The above phenomena led us to the idea of using metallic wires for electromagnetic tunneling applications. Fig.2.1 shows the proposed metallic structure in a parallel plate waveguide geometry similar to what was discussed in section 1.1.2 (Fig.1.3). This geometry consists of two parallel plate waveguides that are parallel to each other and form a 180° bend. Metallic wires are placed at the junction of the waveguides to help transform the energy from one waveguide to the other. The wires are oriented in the y-direction and repeated along the x-direction with displacement of T. These wires connect the two waveguides through holes of radius R centered at distance h from the end of the waveguide. Our results show that TEM modes in one waveguide (with **E** parallel to the wires) can be transmitted to the other waveguide through the wires. The length of the wires, $2l$ can be less than or equal to the total thickness of both waveguides $2a$. The frequency of transmission can be tuned by changing l as we will show later in this chapter.

2.1 Numerical analysis of the structure

We have numerically analyzed the structure using the commercial software Ansoft HFSS full wave simulator. One unit cell of the waveguide containing only one wire is used for the simulation. Perfect magnetic conductor boundary condition is used on the side walls of the waveguides (walls perpendicular to x-axis) to model the entire periodic structure. TEM mode in one waveguide is excited and transmission and reflection coefficients are calculated. Fig.2.2 shows the reflection coefficient (S_{11}) for $a = 3.56mm$, $T = a/10$, $h = T/2$, $r = 40\mu m$ and different values of $t = 2l/2a$ (wire length to waveguide thickness ratio). As seen in the

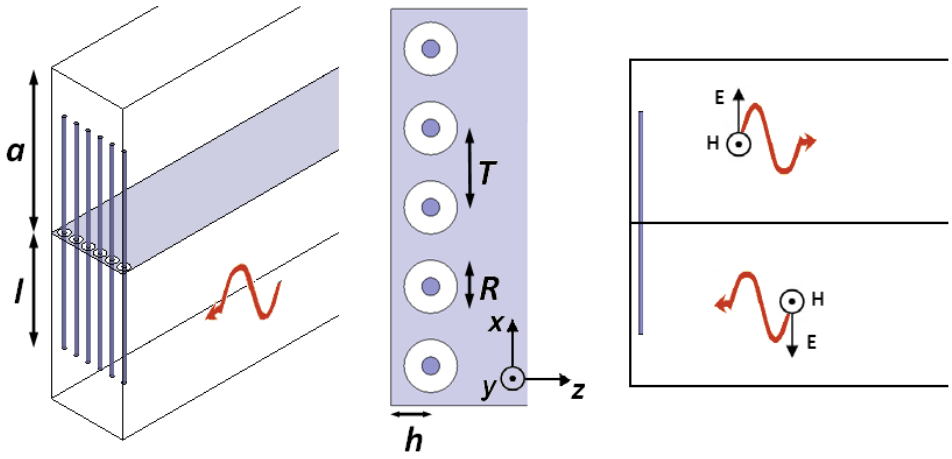

Figure 2.1: Metallic wire structure in parallel plate waveguides

graph, the transmission frequency can be tuned by changing the length of the wires. To explicitly show that the energy is fully transmitted through the wires, we have plotted the transmission coefficient (S_{12}) for the case of $t = 0.7$. Transmission coefficient without the wires is also plotted in Fig.2.2. Note that no transmission is possible through apertures when the metallic wires are not used.

To show that the energy is actually squeezed and transmitted through the wires, the real part of the Poynting vector is plotted in Fig.2.3. The plot shows that all the energy is concentrated in the area between the wires and the conducting wall at the end of the waveguide.

The transmission frequency is mostly sensitive to the length of the wires. Other parameters such as T, h, R, and r do not have a significant effect on the transmission frequency. The bandwidth of the transmission however, depends strongly on T and h. Transmission frequency and 3dB bandwidth for different values of T and h are tabulated in table 2.1. All the other parameters are kept the same as above. Simulations show that the bandwidth increases as T decreases or h increases.

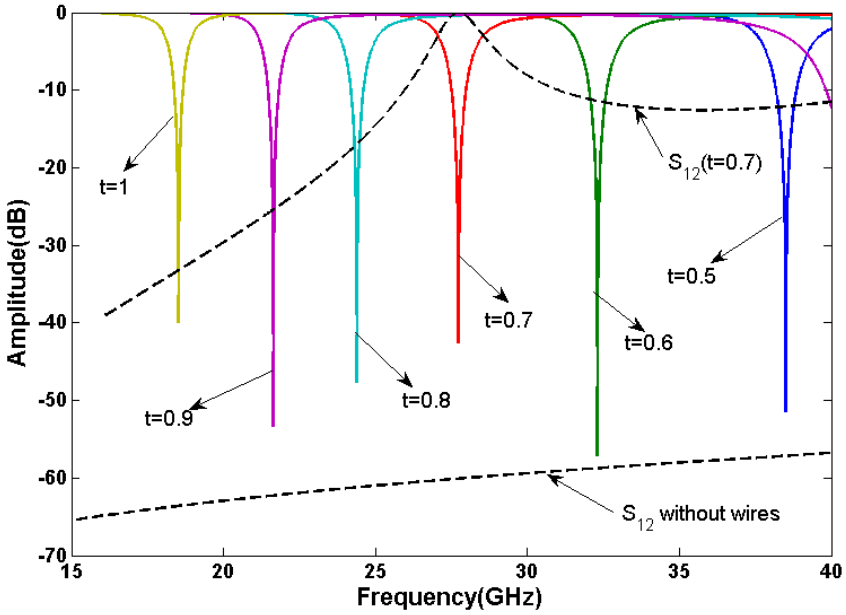

Figure 2.2: Reflection (solid lines) and transmission (dashed lines) coefficient for different values of $t = 2l/2a$.

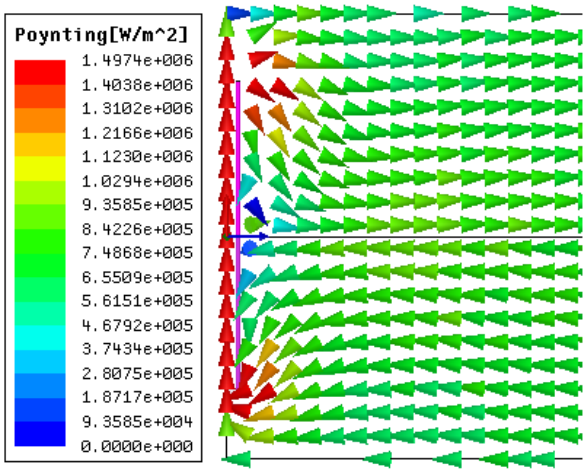

Figure 2.3: The real part of the Poynting vector.

h(μm)	T(μm)	Transmission Frequency (GHz)	3dB Bandwidth (%)
89	187	28.3	2.76
	356	28.46	1.97
	712	28.06	1.14
187	187	27.76	6.05
	356	27.92	4.94
	712	28.22	3.19
356	187	26.4	16.12
	356	26.88	13.09
	712	27.3	9.08

Table 2.1: Transmission frequency and bandwidth for different values of T and h.

Table 2.1 lists the bandwidth and transmission frequency for different values of r and R. It is shown that neither the transmission frequency nor the bandwidth is sensitive to the radius of wires or the holes as long as they are small compared to the wavelength. The radius of wires is important for if the metallic losses are considered. The metallic losses are increased as the radius of wires is decreased. For the above design parameters and copper maid wires of radius $r = 40\mu m$ and dielectric loss tangent of 0.001 (typical value for commonly used dielectrics such as Teflon), total loss is less than 0.5dB. The frequency of transmission for this simulation was around 28Ghz and wires have to be thin in this frequency. Similar simulation for thicker wires at 4Ghz shows negligible loss.

r(μm)	R(μm)	Transmission Frequency (GHz)	3dB Bandwidth (%)
10	60	28.24	4.46
20		27.92	4.94
40		27.70	5.42
20	60	27.92	4.94
	80	27.92	5.01
	120	27.96	5.01

Table 2.2: Transmission frequency and bandwidth for different values of r and R.

2.2 Theoretical analysis of the structure

The structure can be fully analyzed by considering only one unit cell of the structure as shown in Fig.2.4. The walls perpendicular to the x axis are perfect magnetic conductors. Using image theory, this unit cell is identical the infinitely periodic structure of Fig.2.1.

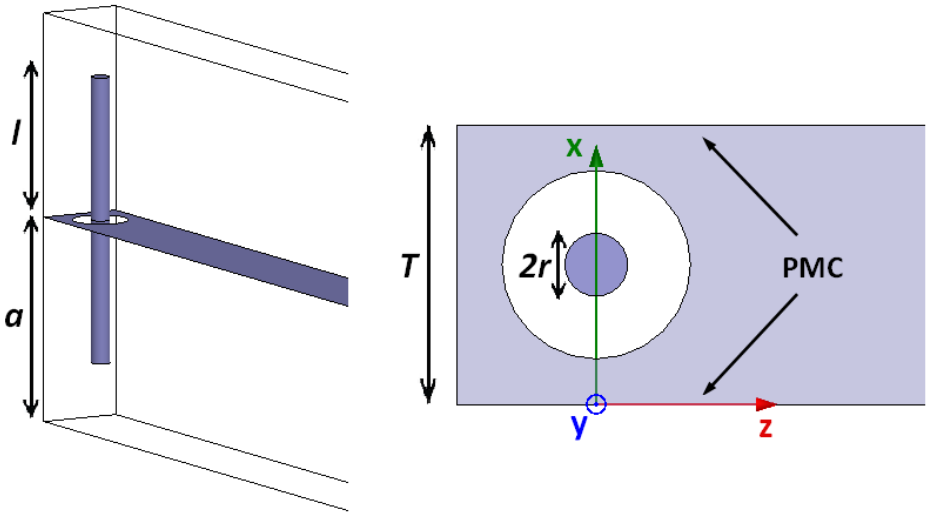

Figure 2.4: One unit cell of the structure.

If we cut the wire in half (in the place of circular aperture) and separate the waveguides, each half of the wire is essentially a probe antenna inside one of the waveguides. These two probes are connected to each other to form the whole structure. Using this analogy, in order for one probe to transmit maximum power to the other prob in the other waveguide, their input impedances have to satisfy this condition: $Z_{in}^{(1)} = (Z_{in}^{(2)})^*$. Also because of the symmetry of the problem, $Z_{in}^{(1)} = Z_{in}^{(2)}$. This can happen only if the imaginary part of the input impedance of each probe is zero. In other words, the transmission frequency is the frequency at witch $Imag(Z_{in}) = 0$. We will use this condition to find the transmission frequency of the structure.

The input impedance of a probe inside a waveguide can be expressed with the following variational formula[19]:

$$Z_{in} = -\frac{1}{I_{in}^2} \iint_S \iint_S \mathbf{J}(\mathbf{r}) \cdot \bar{\mathbf{G}}(\mathbf{r}|\mathbf{r}') \cdot \mathbf{J}(\mathbf{r}') dada' \tag{2.1}$$

where $\bar{\mathbf{G}}(\mathbf{r}|\mathbf{r}')$ is the diadic Green's function and $\mathbf{J}$ is the assumed current distribution on the wires (the true current is unknown at this point). The surface integration is taken

on the surface of the wires . We also assume that $\mathbf{J}$ has only a y component, so we only need G_{yy} component of the dyadic Green's function. The Green's function for a current element inside a waveguide can be expanded in terms of different modes supported by the waveguide[19]:

$$G_{yy} = \frac{jZ_0}{aTk_0} \sum_{n=1}^{\infty}\sum_{m=1}^{\infty} \frac{\epsilon_{0n}\epsilon_{0m}k_m^2}{\Gamma_{nm}} \cos\frac{n\pi x}{T}\cos\frac{n\pi x'}{T}\cos\frac{m\pi y}{a}\cos\frac{m\pi y'}{a} \cdot e^{-\Gamma_{nm}(z_>+h)}\sinh\Gamma_{nm}(z_<+h) \tag{2.2}$$

where $k_m^2 = (m\pi/a)^2 - k_0^2$ and $\Gamma_{nm}^2 = (n\pi/T)^2 + k_m^2$. $z_>$ is the bigger of z and z', and $z_<$ is the smaller of the two. The last two factors in 2.2 can be written as:

$$e^{-\Gamma_{nm}(z_>+l)}\sinh\Gamma_{nm}(z_<+h) = \frac{1}{2}e^{-\Gamma_{nm}|z-z'|} - \frac{1}{2}e^{-2\Gamma_{nm}h-(z+z')\Gamma_{nm}} \tag{2.3}$$

If the radios r of the wires is small compared to wavelength, we can assume $\mathbf{J}$ has a uniform angular distribution:

$$\mathbf{J} = \frac{1}{2\pi r}I(y)\hat{\mathbf{y}} \tag{2.4}$$

Substituting equations 2.2 through 2.4 into 2.1 yields:

$$\begin{aligned} Z_{in} = &-\frac{1}{[I(0)]^2}\left(\frac{jZ_0}{ak_0}\right)\sum_{m=0}^{\infty}\left\{\left[\epsilon_{0m}k_m^2\frac{1}{(2\pi)^2}\iint_0^{2\pi}\left(\sum_{n=0}^{\infty}\frac{\epsilon_{n0}}{2}\frac{\cos\frac{n\pi x}{T}\cos\frac{n\pi x'}{T}}{\Gamma_{nm}T}e^{-\Gamma_{nm}|z-z'|}\right)d\phi d\phi'\right.\right. \\ &\left.\left.-\sum_{n=0}^{\infty}\left(\frac{\epsilon_{0n}\epsilon_{0m}k_m^2}{\Gamma_{nm}T}\right)\frac{1}{(2\pi)^2}\iint_0^{2\pi}\left(\cos\frac{n\pi x}{T}\cos\frac{n\pi x'}{T}e^{-2\Gamma_{nm}h-(z+z')\Gamma_{nm}}\right)d\phi d\phi'\right] \right. \\ &\left.\cdot\left[\int_0^l\cos\frac{m\pi y}{a}I(y)dy\right]\left[\int_0^l\cos\frac{m\pi y'}{a}I(y')dy'\right]\right\} \end{aligned} \tag{2.5}$$

In order to be able to integrate the series around the circumference of the probe, and also to obtain a more rapidly converging series we use the following formula:

$$\begin{aligned} &\sum_{n=0}^{\infty}\frac{\epsilon_{n0}}{2}\frac{\cos\frac{n\pi x}{T}\cos\frac{n\pi x'}{T}}{\Gamma_{nm}T}e^{-\Gamma_{nm}|z-z'|} \\ &\quad= -\frac{j}{4}H_0^2(-jk_m\sqrt{(x-x')^2+(z-z')^2}) \\ &\quad\quad -\frac{j}{4}H_0^2(-jk_m\sqrt{(x+x')^2+(z-z')^2}) \\ &\quad\quad -\frac{j}{4}\sum_{n=-\infty}^{\infty}{}'[H_0^2(-jk_m\sqrt{(x-x'-2nT)^2+(z-z')^2}) \\ &\quad\quad +H_0^2(-jk_m\sqrt{(x+x'+2nT)^2+(z-z')^2})] \end{aligned} \tag{2.6}$$

The prime on the summation means that $n = 0$ is excluded from the sum. In all terms but the first, the argument of the Hankel function is big enough that we can neglect the ϕ variation and put $x = x' = T/2$ and $z = z' = 0$. In the first term we use $x = (T/2) + r\cos\phi, z = r\sin\phi$ and similar expressions for x' and z'. After simplification and using the relationship between Hankel function and the modified bessel function of the second kind K_0 we get:

$$\sum_{n=0}^{\infty} \frac{\epsilon_{n0}}{2} \frac{\cos\frac{n\pi x}{T}\cos\frac{n\pi x'}{T}}{\Gamma_{nm}T} e^{-\Gamma_{nm}(z_>+l)} \tag{2.7}$$
$$= \frac{1}{2\pi}\left\{K_0\left(2k_m r\left|\sin\frac{\phi-\phi'}{2}\right|\right) + \sum_{n=1}^{\infty} 2K_0(k_m nT)\right\}$$

The second term (summation) does not change with ϕ or ϕ'. The integration of the first term over ϕ and ϕ' is given by:

$$\frac{1}{(2\pi)^2}\iint_0^{2\pi} K_0\left(2k_m r\left|\sin\frac{\phi-\phi'}{2}\right|\right) d\phi d\phi' = I_0(k_m r)K_0(k_m r) \tag{2.8}$$

which is obtained by using $u = \sin(\phi-\phi')/2$ and

$$\int_0^1 \frac{K_0(2k_m ru)}{\sqrt{1-u^2}} dx = \frac{\pi}{2} I_0(k_m r)K_0(k_m r) \tag{2.9}$$

where I_0 is the modified bessel function of the first kind. The bessel function series in 2.7 converge rapidly if $m > 0$, but for $m = 0$, $k_m = -jk_0$ and the series will turn to a slowly converging Hankel function series and we have to modify 2.6. We can use $x = x' = T/2$ for all terms but the first. We also use $z = r\sin\phi$ and $z' = r\sin\phi'$ for the first term and $z' = z = r$ for all other terms. After averaging over ϕ and ϕ' we have[19]:

$$\begin{aligned} &-\frac{j}{4}[J_0(k_0 r) - 1]H_0^2(k_0 r) - \frac{j}{4}H_0^2(k_0 r) - \frac{j}{4}H_0^2(k_0\sqrt{(a^2+r^2)}) \\ &-\frac{j}{4}\sum_{n=-\infty}^{\infty}{}'[H_0^2(k_0\sqrt{(2nT)^2+r^2}) + H_0^2(k_0\sqrt{((2n+1)T)^2+r^2})] \\ =&-\frac{j}{4}[J_0(k_0 r) - 1]H_0^2(k_0 r) + \sum_{n=0,2,\ldots}^{\infty}\left(\frac{\epsilon_{0n}}{2}\frac{e^{-\Gamma_{n0}r}}{\Gamma_{n0}T}\right) \end{aligned} \tag{2.10}$$

The series in this equation can be written in terms of a more rapidly converging series:

$$\begin{aligned} \sum_{n=0,2,\ldots}^{\infty}\left(\frac{\epsilon_{0n}}{2}\frac{e^{-\Gamma_{n0}r}}{\Gamma_{n0}T}\right) &= \frac{1}{2}\frac{e^{-jk_0 r}}{jk_0 r} + \sum_{n=2,4,\ldots}^{\infty}\left(\frac{e^{-n\pi r/a}}{n\pi}\right) + \sum_{n=2,4,\ldots}^{\infty}\left(\frac{e^{-\Gamma_{n0}r}}{\Gamma_{n0}T} - \frac{e^{-n\pi r/a}}{n\pi}\right) \\ &= \frac{1}{2}\frac{e^{-jk_0 r}}{jk_0 r} - \frac{1}{2\pi}ln\left(1-e^{-2\pi r/a}\right) + \sum_{n=2,4,\ldots}^{\infty}\left(\frac{e^{-\Gamma_{n0}r}}{\Gamma_{n0}T} - \frac{e^{-n\pi r/a}}{n\pi}\right) \end{aligned} \tag{2.11}$$

The second term in 2.5 has the factor

$$\cos\frac{n\pi x}{T}\cos\frac{n\pi x'}{T}e^{-2\Gamma_{nm}h-(z+z')\Gamma_{nm}} \tag{2.12}$$

For these terms we use $x=(T/2)+r\cos\phi, z=r\sin\phi$ and similar expressions for x' and z'. The averaging of this factor over ϕ and ϕ' is zero for odd ns. For even numbers we get:

$$e^{-2\Gamma_{nm}h}\left[1-\left(\frac{n\pi}{T}\right)^2\frac{r^2}{2}(\cos^2\phi+\cos^2\phi')+\Gamma_{nm}^2\frac{r^2}{2}(\sin\phi+\sin\phi')^2-\Gamma_{nm}r(\sin\phi+\sin\phi')\right]$$

to order r^2. The averaging over ϕ and ϕ' gives

$$e^{-2\Gamma_{nm}h}\left[1+\left(\Gamma_{nm}^2-\frac{n^2\pi^2}{T^2}\right)\frac{r^2}{2}\right]=e^{-2\Gamma_{nm}h}\left(1+k_m^2\frac{r^2}{2}\right) \tag{2.13}$$

Now we can rewrite equation 2.5 in this form

$$Z_{in}=-\frac{1}{[I(0)]^2}\sum_{m=0}^{\infty}g_m\left(\int_0^l\cos\frac{m\pi y}{a}I(y)dy\right)\left(\int_0^l\cos\frac{m\pi y'}{a}I(y')dy'\right) \tag{2.14}$$

where g_m $(m>0)$ is calculated as

$$\begin{aligned}g_m=&\left(\frac{jZ_0}{ak_0}\right)\left(\frac{k_m^2}{\pi}\right)\left(I_0(k_mr)K_0(k_mr)+\sum_{n=1}^{\infty}2K_0(k_mnT)\right)\\&-\left(\frac{jZ_0}{ak_0}\right)\left(1+k_m^2\frac{r^2}{2}\right)\left(\frac{k_m}{T}e^{-2k_mh}+2k_m^2\sum_{n=2,4,\ldots}^{\infty}\frac{e^{-2\Gamma_{nm}h}}{\Gamma_{nm}T}\right)\end{aligned} \tag{2.15}$$

and

$$\begin{aligned}g_0=&-\left(\frac{jZ_0k_0}{a}\right)\left[-\frac{j}{4}(J_0(k_0r)-1)H_0^2(k_0r)\right.\\&+\frac{1}{2}\frac{e^{-jk_0r}}{jk_0r}-\frac{1}{2\pi}ln\left(1-e^{-2\pi r/a}\right)+\left.\sum_{n=2,4,\ldots}^{\infty}\left(\frac{e^{-\Gamma_{n0}r}}{\Gamma_{n0}T}-\frac{e^{-n\pi r/a}}{n\pi}\right)\right]\\&+\left(\frac{jZ_0k_0}{a}\right)\left(1-k_0^2\frac{r^2}{2}\right)\left(\frac{e^{-2jk_0h}}{2jTk_0}+\sum_{n=2,4,\ldots}^{\infty}\frac{e^{-2\Gamma_{n0}h}}{\Gamma_{n0}T}\right)\end{aligned} \tag{2.16}$$

In order to find the best choice for the assumed current on the wires, we use a set of basis functions $\psi_\nu(y)$ to form $I(y)$:

$$I(y)=\sum_{\nu=1}^{q}I_\nu\psi_\nu(y) \tag{2.17}$$

We define $P_\nu^{(m)}$ as

$$P_\nu^{(m)} = \int_0^l \cos\frac{m\pi y}{a}\psi_\nu(y)dy \tag{2.18}$$

If we normalize ψ_ν so that $\psi_\nu(0) = 1$ then $I(0) = \sum_{\nu=1}^{p} I_\nu$ and 2.14 can be written in the following matrix format:

$$Z_{in} = -\frac{\mathbf{I}^T\mathbf{G}\mathbf{I}}{\mathbf{I}^T\mathbf{N}\mathbf{I}} \tag{2.19}$$

where

$$\mathbf{I} = [I_1 I_2 ... I_q]^T, \tag{2.20}$$

$$[\mathbf{G}]_{ij} = \sum_{m=0}^{\infty} g_m P_i^{(m)} P_j^{(m)}, \tag{2.21}$$

$$[\mathbf{N}]_{ij} = 1 \tag{2.22}$$

The coefficients I_1 to I_p are still to be determined. The best approximation for Z_{in} is given when the formula is stationary ($\partial Z_{in}/\partial I_j = 0$), so the vector $\mathbf{I}$ is the solution to the equation

$$\frac{d}{d\mathbf{I}}Z_{in} = -2\frac{(\mathbf{I}^T\mathbf{G}\mathbf{I})(\mathbf{I}^T\mathbf{N}) - (\mathbf{I}^T\mathbf{N}\mathbf{I})(\mathbf{I}^T\mathbf{G})}{(\mathbf{I}^T\mathbf{N}\mathbf{I})^2} = 0 \tag{2.23}$$

that can be solved using numerical methods. We selected the following four basis functions to solve the problem:

$$\psi_1 = \frac{\sin k_0(l-y)}{\sin k_0 l} \tag{2.24}$$

$$\psi_2 = \frac{1-\cos k_0(l-y)}{1-\cos k_0 l} \tag{2.25}$$

$$\psi_3 = \cos\frac{\pi y}{2l} \tag{2.26}$$

$$\psi_4 = \cos\frac{3\pi y}{2l} \tag{2.27}$$

The results are shown in Fig.2.5 and compared with the HFSS simulation results of previous section. The difference between the two results are less than five percent in the worst case. The theoretical results are approximate and simulation results should be trusted. However, the time required to generate theoretical results is much less than the time required to run the simulations. An appropriate design procedure would be to find the approximate design parameters theoretically and make small corrections using numerical simulation. The MATLAB code that we used to generate the theoretical results is provided in the appendix.

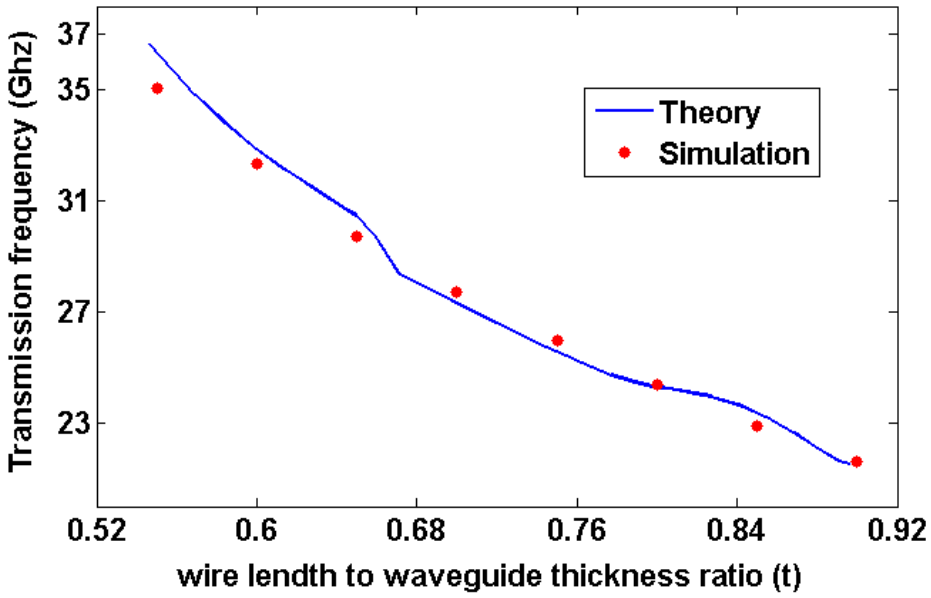

Figure 2.5: Theoretical results of transmission frequency for different wire lengthes and comparison with simulation.

Chapter 3

Metallic Wires in different Geometries

In addition to the 180° bend structure that was analyzed in previous chapter, metallic wires show tunneling effect in many other 2D and 3D geometries. In this chapter, we will discuss some of these geometries.

3.1 The U-Shaped Narrow Channel

Fig.3.1 shows the metallic wires in the geometry of a U-shaped narrow channel. This geometry is similar to what was discussed in section 1.1.2 (Fig.1.5). It was shown that electromagnetic waves can be transmitted through the channel if filled with ENZ materials. In this section we will discuss the case where metallic wires are used in the channel.

The geometry consists of two parallel plate waveguides that are connected to each other with a narrow U-shaped channel. Wires are placed parallel to the ending wall of the waveguides, then they bend and continue their way all the way through the narrow channel(Fig.3.1). The length of the free part of the wires, l plays the key roll in tuning the transmission frequency. Unlike the 180° geometry that we discussed in previous chapter, waves can be fully transmitted through the narrow channel in certain frequencies depending on the exact geometry of the channel(Fig.1.6). These transmission are due to fabry-perot type resonances and cannot be tuned independent of the length of the channel. For the metallic wires, the length of the free part of the wires can be tuned to transmit the energy at the desired frequency. We have tuned the wires to work at 26GHz for different channel lengthes. Results are shown in Fig.3.3.

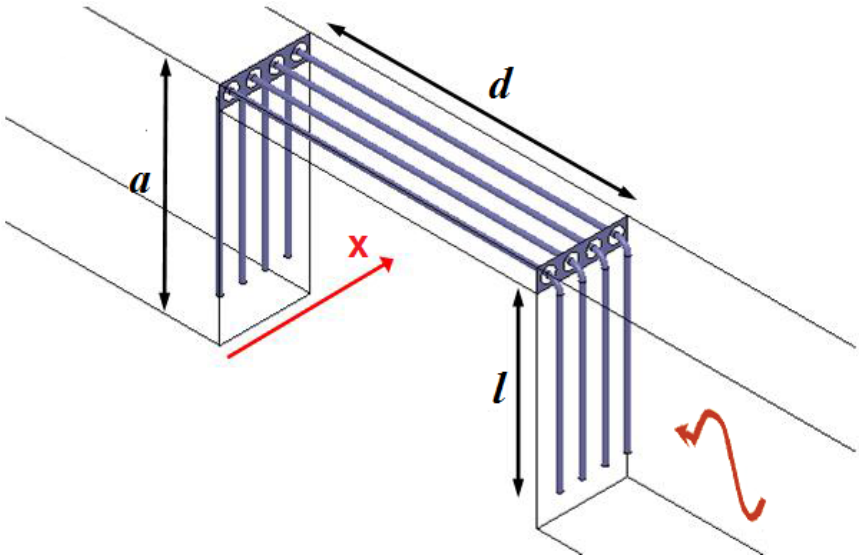

Figure 3.1: The U-shaped Narrow channel geometry

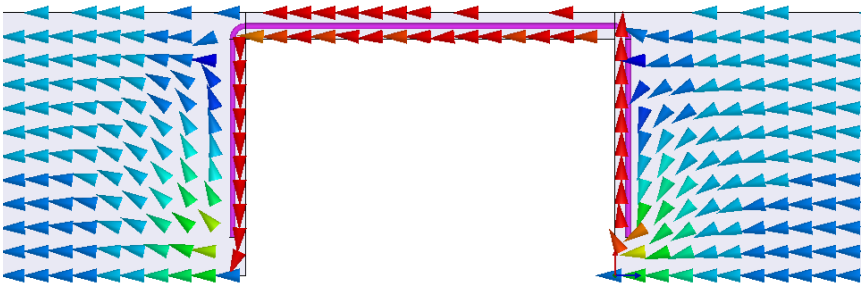

Figure 3.2: The real part of Poyning vector in the structure.

The wire and the conductor plane at the end of the waveguide behave like a transmission line. At the transmission frequency, the energy is fully coupled to this transmission line and propagates along the wires to the other side of the channel. The real part of the Poynting vector is plotted in fig.3.2 and confirms the confinement and transmission of energy along the wires.

Similar to the 180° bend structure that was discussed in the previous chapter, the bandwidth of transmission in narrow U-shaped channel highly depends on h. Changing h also changes the transmission frequency, but the transmission frequency is much more sensitive to the length of the wires than h. In the design procedure, h is designed for the desired bandwidth and the shift in transmission frequency is compensated with a slight

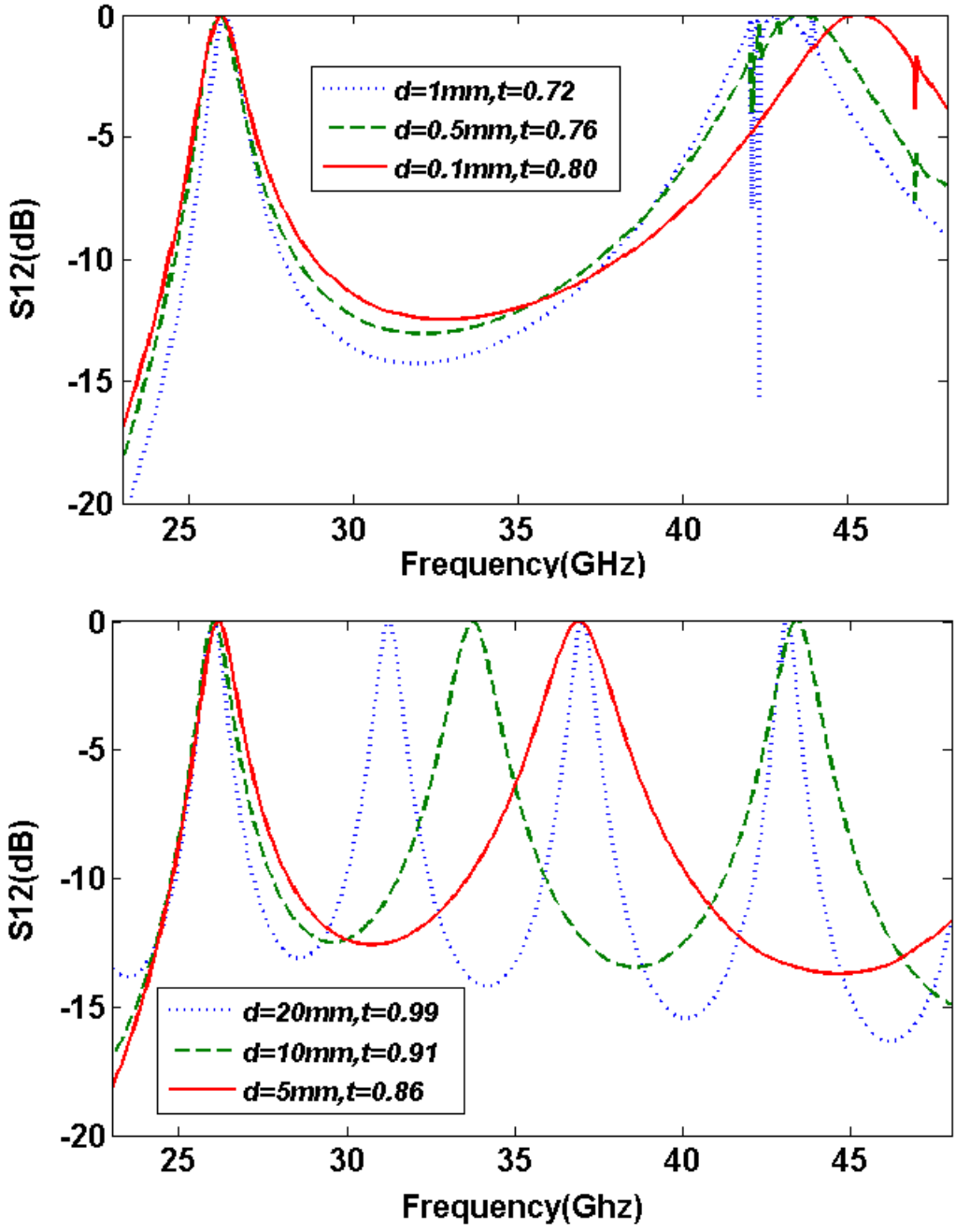

Figure 3.3: Transmission coefficient for different channel lengthes.

variation in the length of the wires. The transmission frequency and the 3dB bandwidth for different values of h and the thickness of the channel a_{ch} are listed in table 3.1. The simulations show that the bandwidth is increased significantly as h is increased. Increasing the thickness of the channel, a_{ch} decreases the bandwidth but the bandwidth is much less sensitive the thickness of the channel than h.

h(μm)	$a_{ch}(\mu m)$	Transmission Frequency (GHz)	3dB Bandwidth (%)
89	187	28.76	1.11
	356	28.86	0.97
	712	28.86	0.76
187	187	27.8	3.53
	356	27.64	3.98
	712	27.92	2.79
356	187	26.22	10.98
	356	25.74	10.18
	712	25.08	9.65

Table 3.1: Transmission frequency and bandwidth for different values of a_{ch} and h.

In addition to the transmissions due to coupling to the wires, fabry-perot type transmissions may happen at different frequencies. Fabry-perot transmissions are due to the multiple reflections from the two apertures of the narrow channel. The frequency at which a fabry-perot resonance happens depends on the length of the channel and the size and shape of the aperture and cannot be tuned independent of the geometry of the channel. Fig.3.4 shows the transmission and reflection coefficients of the U-shaped narrow channel with metallic wires and no hole in the aperture of the channel (rectangular aperture). There are two different transmissions at $f_1 = 25.56Ghz$ and $f_2 = 26.48Ghz$. The real part of the Poynting vector at each frequency is given in fig.3.5 and fig.3.6 respectively. It is seen that at the fabry-parot resonance frequency ($f = 25.56Ghz$) the energy is mostly transferred through the aperture whereas at $f = 26.48Ghz$ the energy is coupled to the wires and is transmitted. The main difference between the two types of resonance is that the coupling between the wires can be tuned for the desired frequency but this is not the case for fabry-perot resonances.

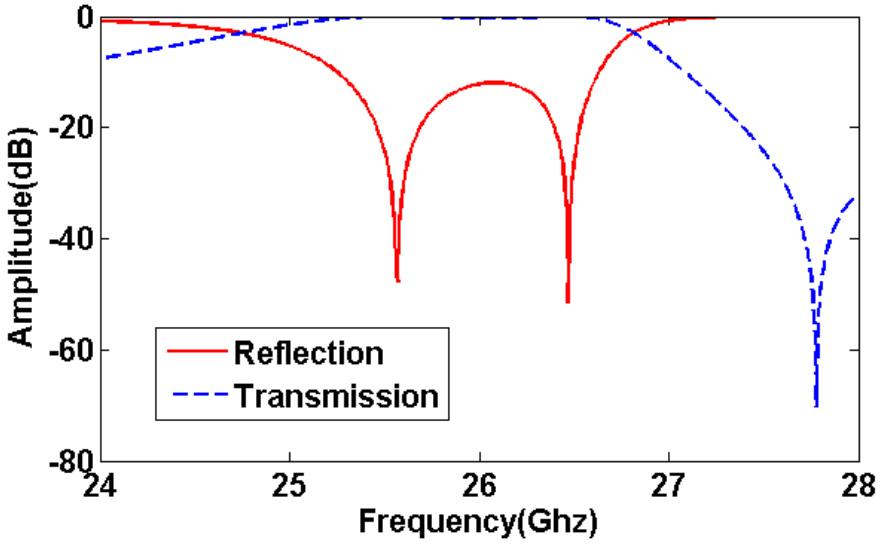

Figure 3.4: Transmission (dashed line) and reflection (solid line) coefficients for the channel with a rectangular aperture.

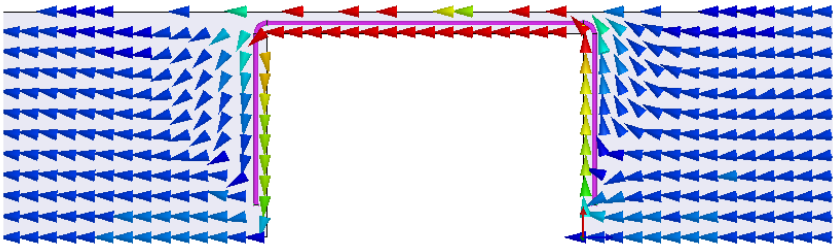

Figure 3.5: The real part of Poyning vector at $f = 25.56Ghz$.

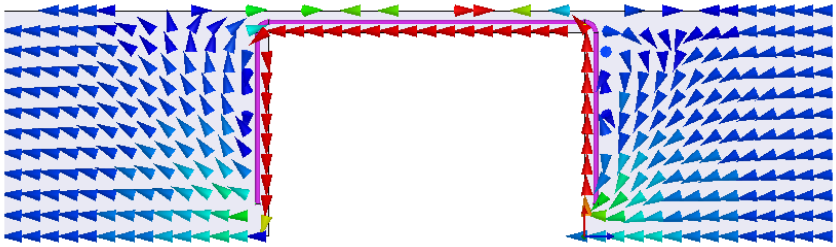

Figure 3.6: The real part of Poyning vector at $f = 26.48Ghz$.

3.2 Bends of different Angels

Metallic wires can be used to transfer energy in waveguide bends of any angle. Fig.3.7 shows the cross-section of a 140° bend in a parallel plate waveguide. This geometry is similar to the parallel plate waveguide that was introduced in the previous chapter except the wires are bent in the place of the circular aperture. The reflection coefficient for different bend angles is plotted in Fig.3.8. All the dimensions are the same as the previous chapter (i.e. $a = 3.56mm$, $T = a/10$, $r = 40\mu m$ and $R = 3r$) and the length of the straight part of the wire is $l = 0.75a$. As seen in F=fig.3.8, the transmission frequency is different for different bend angles. This frequency shift is due to the change in the length of the wire when it is bent .We have kept the length of the straight part of the wire, but the length of the curved part of it will change with the angel. The transmission frequency at each angel can indeed be tuned as desired by changing the length of the straight part of the wires. In fig.3.9, we have shown the real part of the Poynting vector for the bend angel of 90°. The graph shows that the energy is squeezed and transmitted between the two waveguides.

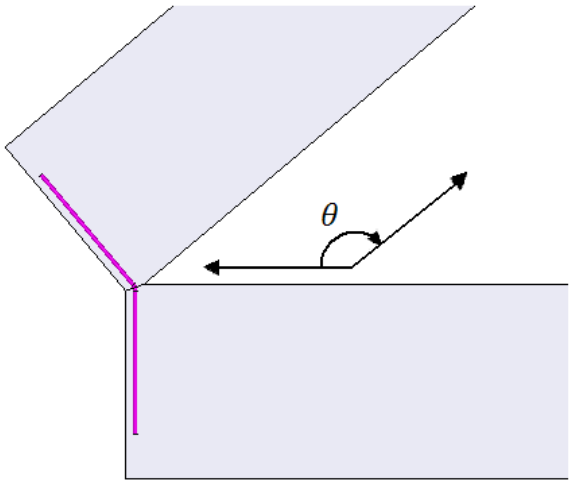

Figure 3.7: Geometry of a parallel plate waveguide bend with the angel θ

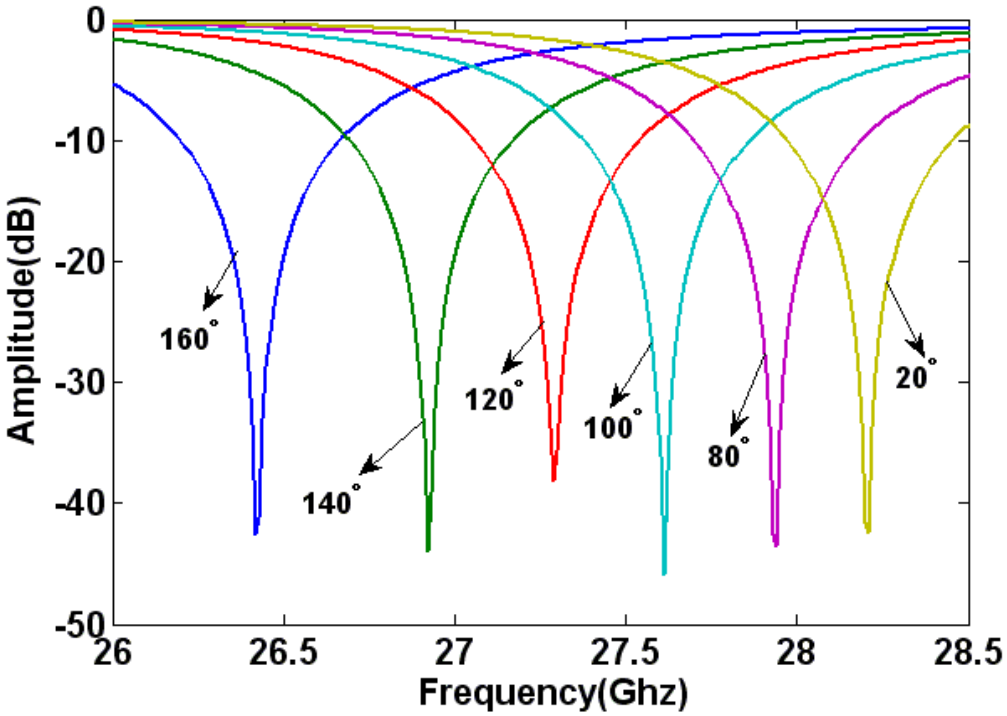

Figure 3.8: Reflection coefficient for bends of different angles.

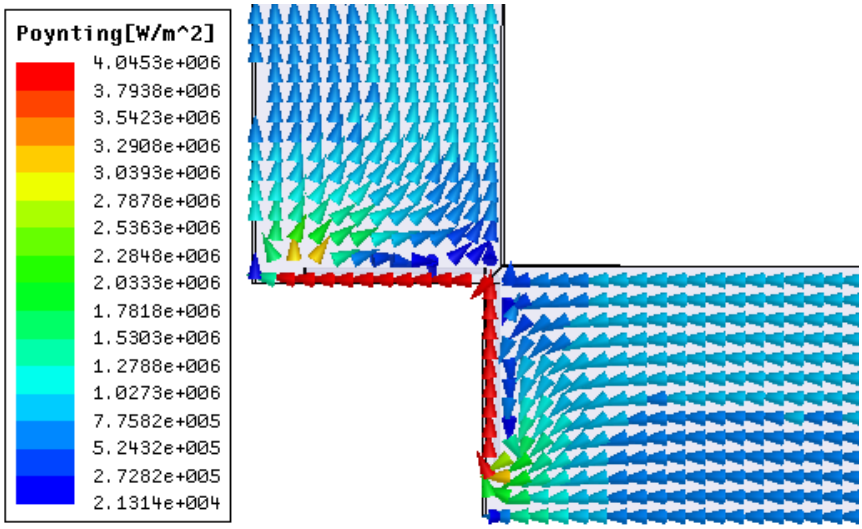

Figure 3.9: The real part of Poynting vector inside the structure.

3.3 3D Waveguide Geometries

Consider the parallel plate geometry of previous chapter (fig.2.1), with the exception that only a finite number of wires are used and waveguides are truncated on both edges with metallic walls perpendicular to x-direction, thus forming a rectangular waveguide bend of 180°. Fig.3.10 shows the geometry and a snapshot of the magnitude of electric field in the waveguide when the TE_{01} mode of the bottom waveguide is excited. The length of the wires l is equal to thickness of the waveguide $a = 12.7mm$ and the width W of the waveguide is 10 times the separation of the wires ($W = 10T$). The radius of the wires $r = 0.5mm$ and the radius of the circular apertures $R = 3r$. The reflection and transmission coefficients are calculated using Ansoft HFSS full wave simulator and is plotted in fig.3.11. Note that the bandwidth of this structure is much better than what was reported in [14] using waveguide in cutoff.

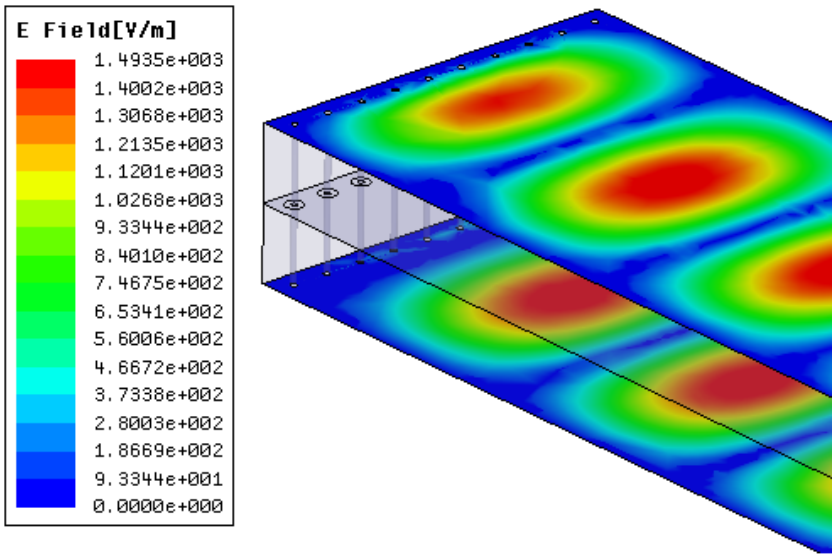

Figure 3.10: The 180° in a rectangular waveguide and a snapshot of the electric field.

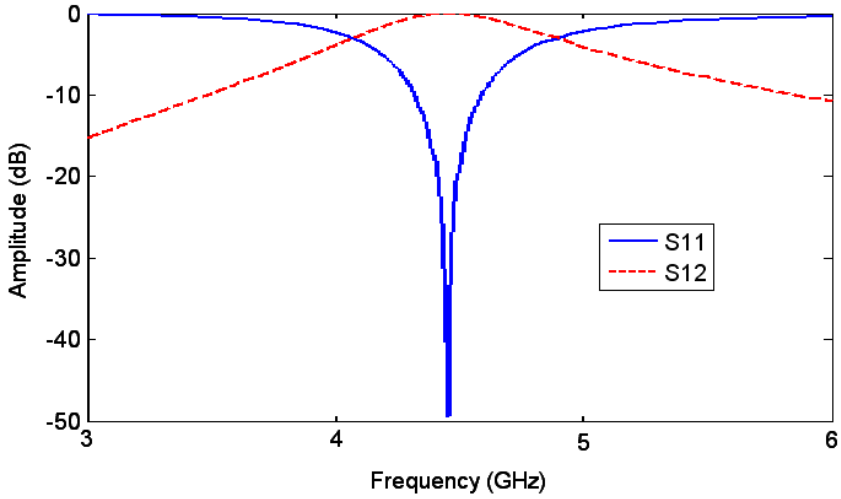

Figure 3.11: Transmission and reflection coefficients for the rectangular waveguide bend.

3.4 Experimental Verification of Tunneling in Metallic Wires

We have fabricated the three dimensional 180^0 bend structure that was mentioned in section 3.3 using plexiglass($\epsilon = 2.57$) covered by copper sheets. The thickness of the waveguide $a = 17mm$ and the width of the waveguide $T = 63.5mm$. Metallic wires are made of steel with dimensions of $l = 10mm$, $r = 1/16in$ and $R = 3r$, and periodicity of , $T = 12.7mm$. We also built a control waveguide with the same dimensions as the original one but without any bend or wire. The waveguide feed is a probe antenna that is connected to a vector network analyzer (Agilent HP8722ES) via a 50 ohm coaxial cable. The measured transmission coefficients for both control and bent waveguides are plotted in fig. 3.12. As seen in the graph, there is about $1.5dB$ loss at transmission frequency (4GHz) in the control waveguide. This is due to feed impedance mismatch and dielectric losses. There is also imperfection in the construction of waveguide walls especially for the bent waveguide and we think this is the reason why there is about $2.5dB$ loss in the bent waveguide measurements. Our simulation, however, shows negligible loss even when metallic and dielectric losses are considered (the dashed line in fig. 3.12). Fig.3.13 shows the experimental setup that we used for our measurements.

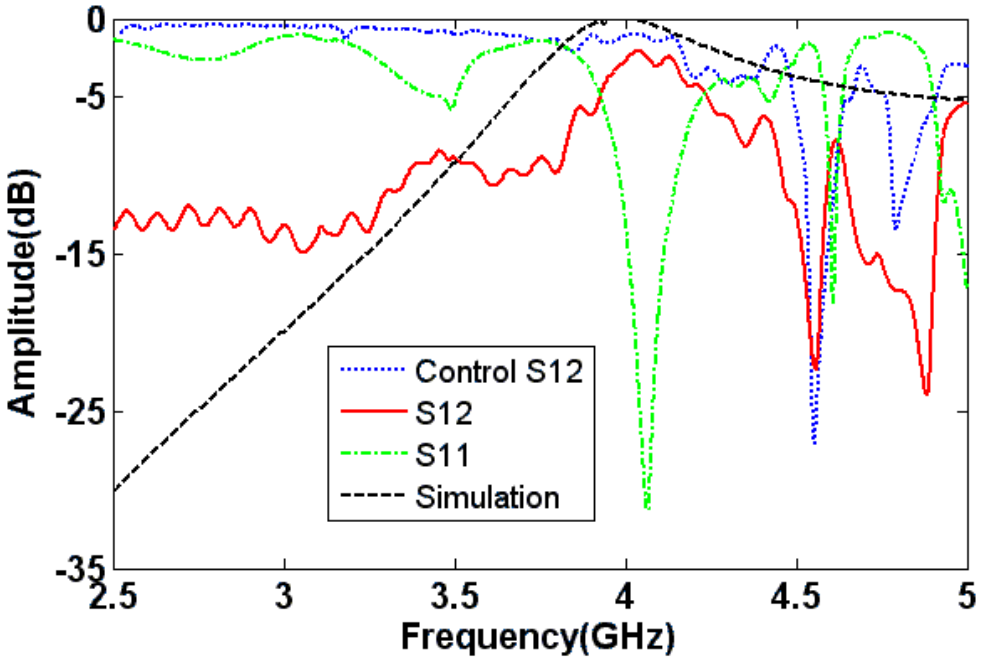

Figure 3.12: Transmission coefficient for the bent waveguide(solid line), the control waveguide (dotted line) and simulation (dashed line)

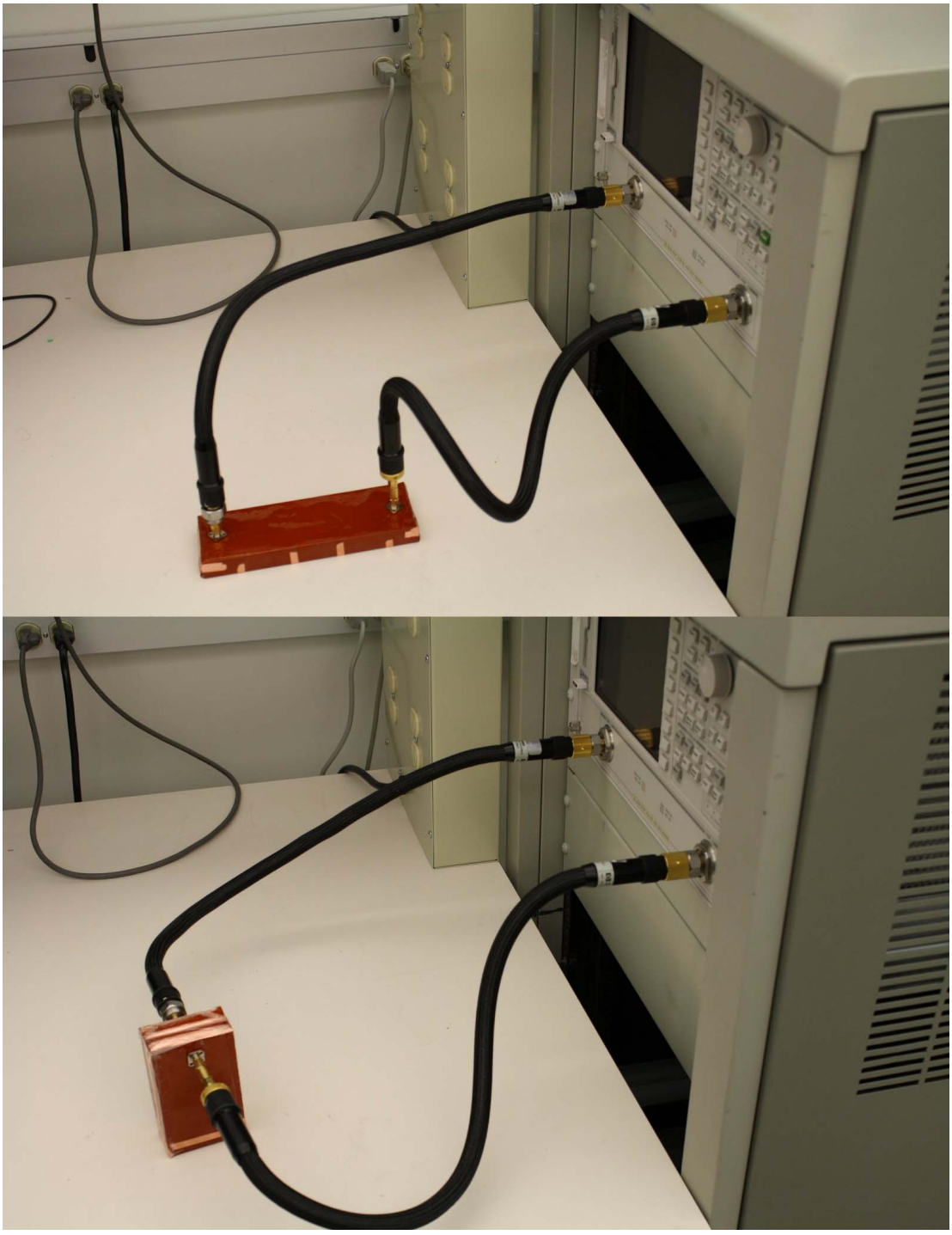

Figure 3.13: Experimental setups.

Chapter 4

Summary and Future Research

4.1 Summary

A new structure that allows for electromagnetic energy squeezing and transmission trough narrow channels and waveguide junctions and bends was introduced in this thesis. The performance of the structure was theoretically analyzed and numerically tested in a number of waveguide geometries with different junction shapes. It was shown that the wire structure is capable of transmitting energy in different waveguide discontinuities and bends and the frequency of transmission can be tuned independent of the dimensions of the junction. The wires structure was compared to other methods of squeezing and transmitting energy especially transmission using materials with extremely small permittivity. The primary advantage of the structure proposed here is in its simple construction, low cost, low loss and wider bandwidth in comparison to what was reported earlier.

4.2 Future Research

In addition to investigation on achieving better transmission properties such as higher bandwidth or extending the range of frequencies to infrared or optical frequencies, other possible applications of the proposed structure can be subject of future research. Some of the areas where this structure may be suitable to use include sensing, de-multiplexing and power dividing.

- *Sensing*
  When the energy is squeezed into a narrow area the magnitude of electric field will be increased dramatically. It is shown in [20] that highly concentrated electromagnetic

field allows for very sensitive measurements of changes in the dielectric constant of the material inside the channel.

- *De-multiplexing*
  Metallic wires structure can transfer energy from one waveguide to another in a certain frequency. It might be possible to use more than one wire length to transfer different frequency components of the signal to different receiving waveguides, thus de-multiplexing the signal in frequency domain.

APPENDICES

Appendix A

the MATLAB code for finding the transmission frequency

```
1
2  clear
3  fmin=20;
4  fmax=23;
5
6  %————————————————————— Problem Parameters—————————————————————
7
8  fract=0.9;                % wire length to waveguide thickness ratio
9  b=3.56e-3;                % thickness of the waveguide
10 a=2*0.178e-3;             % periodicity
11 r=40e-6;                  % radius of the wires
12 d=fract*3.56e-3;          % half of the lenghth of the wires
13 l=0.178e-3;               % distance from the end of the waveguide
14
15 %————————————————————— General Parameters —————————————————————
16
17 mu=4*pi*1e-7;             % permeability
18 eps=8.85e-12;             % permitivity
19 Z0=sqrt(mu/eps);          % Impedace
20
21 ncount=10;                % number of series elements calculated
22 mcount=10;
23 m=1:mcount;
24 en=2:2:2*ncount;
25 n=1:scount;
26 Zin=[];fr=[];
27
28
```

```
%------------------------------ Body of Program ------------------------------

for Freq=fmin:0.01:fmax,

 k0=2*pi*Freq*1e9*sqrt(eps*mu);
 km=sqrt((m*pi/b).^2-k0^2);
 Gammaen0=sqrt((en*pi/a).^2-k0^2);
 Gammanm=sqrt(repmat([(en*pi/a).^2]',[1,numel(m)])+...
             repmat(km.^2,[numel(en),1]));

%-------------------- Current Basis Function Parameters ---------------------

 Q0=(1-cos(k0*d))/(k0*sin(k0*d));
 Q=k0*(cos(k0*d)-cos(m*pi*d/b))./(km.^2*sin(k0*d));

 P0=(k0*d-sin(k0*d))/(k0*(1-cos(k0*d)));
 P=(k0*sin(k0*d)-(k0^2*b./(pi*m)).*sin(m*pi*d/b))./(km.^2*(1-cos(k0*d)));

 R0=2*d/pi;
 R=(2*b^2*d/pi)*cos(pi*d*m/b)./(b^2-4*d^2*m.^2);

 S0=2*b/(3*pi);
 S=(6*b^2*d/pi)*cos(pi*d*m/b)./(9*b^2-4*d^2*m.^2);

%----------------------- Green Function Parameters ----------------------------

 g0=(j*Z0/(b*k0))*(-k0^2)*(...
                          (-j/4)*(besselj(0,k0*r)-1)*besselh(0,2,k0*r)+...
                          (1/2)*(exp(-j*k0*r)/(j*k0*r))+...
                          (-1/(2*pi))*log(1-exp(-2*pi*r/a))+...
                          sum(exp(-r*Gammaen0)./(Gammaen0&a)-...
                          exp(-en*pi*r/a)./(pi*en))...
                           )+...
    (-j*Z0/(b*k0))*(1-k0^2*r^2/2)*(...
                     (-k0^2/(2*a*j*k0))*exp(-2*j*k0*l)+...
                     sum((-k0^2./(a*Gammaen0)).*exp(-2*Gammaen0*l))...
                      );

 gm=(j*Z0/(b*k0))*(km.^2/pi).*(...
                                besseli(0,km*r).*besselk(0,km*r)+...
                                sum(2*besselk(0,a*((n')*km)))...
                                )+...
    (-j*Z0/(b*k0))*(...
                     (km/a).*exp(-2*km*l).*(1+km.^2*r^2/2)+...
                     (2*km.^2).*(1+km.^2*r^2/2).*...
                     sum(exp(-2*Gammanm*l)./(a*Gammanm))...
                     );

```

```
77  G11=g0*P0^2+sum(gm.*(P.^2));
78  G22=g0*Q0^2+sum(gm.*(Q.^2));
79  G33=g0*R0^2+sum(gm.*(R.^2));
80  G44=g0*S0^2+sum(gm.*(S.^2));
81
82  G12=g0*P0*Q0+sum(gm.*P.*Q);
83
84  G13=g0*P0*R0+sum(gm.*P.*R);
85  G23=g0*Q0*R0+sum(gm.*Q.*R);
86
87  G14=g0*P0*S0+sum(gm.*P.*S);
88  G24=g0*Q0*S0+sum(gm.*Q.*S);
89  G34=g0*R0*S0+sum(gm.*R.*S);
90
91  G=[G11,G12,G13,G14;...
92     G12,G22,G23,G24;...
93     G12,G23,G33,G34;...
94     G14,G24,G34,G44];
95
96  N=[1,1,1,1;1,1,1,1;1,1,1,1;1,1,1,1];
97
98  I0=1./(2*diag(G)-sum(G,2));
99  I=fsolve(@(x) derfun(x,G,N),I0); % numerical solution of dz/di=0
100 Zin=[Zin,-(I'*G*I)/(I'*N*I)];
101 fr=[fr,Freq];
102
103 end
104
105 [mn,ind]=min(abs(imag(Zin)));
106 trf=fr(ind)
107
```

```
1
2  function y=derfun(x,G,N),
3  y=abs(((x'*G*x).*(N*x)-(x'*N*x).*(G*x))./(x'*G*x)^2);
4
```

References

[1] Engheta N. Silveirinha, M. Tunneling of electromagnetic energy through subwavelength channels and bends using -near-zero materials. *Physical Review Letters*, 97(15), 2006. ix, 1, 2, 3, 5, 6, 10

[2] Engheta N. Silveirinha, M.G. Theory of supercoupling, squeezing wave energy, and field confinement in narrow channels and tight bends using near-zero metamaterials. *Physical Review B - Condensed Matter and Materials Physics*, 76(24), 2007. ix, 1, 6, 7, 8

[3] Alu A. Young M.E. Silveirinha M. Engheta N. Edwards, B. Experimental verification of epsilon-near-zero metamaterial coupling and energy squeezing using a microwave waveguide. *Physical Review Letters*, 100(3), 2008. ix, 1, 11

[4] Alu A. Young M.E. Silveirinha M. Engheta N. Edwards, B. Experimental verification of epsilon-near-zero metamaterial coupling and energy squeezing using a microwave waveguide. *Physical Review Letters*, 100(3), 2008. ix, 1, 12, 13, 14

[5] Garcea-Vidal F.J. Lezec H.J. Pellerin K.M. Thio T. Pendry J.B. Ebbesen T.W. Marten-Moreno, L. Theory of extraordinary optical transmission through subwavelength hole arrays. *Physical Review Letters*, 86(6):1114–1117, 2001. 1

[6] Zakharian A.R.-Moloney J.V. Mansuripur M. Xie, Y. Transmission of light through slit apertures in metallic films. *Optics Express*, 12(25):6106–6121, 2004. 1

[7] Enoch S.-Li L. Popov E. Neviere M. Bonod, N. Resonant optical transmission through thin metallic films with and without holes. *Optics Express*, 11(5):482–490, 2003. 1

[8] Lezec H.J.-Ebbesen T.W. Pellerin K.M. Lewen G.D. Nahata A. Linke R.A. Thio, T. Giant optical transmission of sub-wavelength apertures: Physics and applications. *Nanotechnology*, 13(3):429–432, 2002. 1

[9] J.B. Pendry. Negative refraction makes a perfect lens. *Physical Review Letters*, 85(18):3966–3969, 2000. 1

[10] Belov P.A.-Simovski C.R. Silveirinha, M.G. Subwavelength imaging at infrared frequencies using an array of metallic nanorods. *Physical Review B - Condensed Matter and Materials Physics*, 75(3), 2007. 1

[11] M.I. Stockman. Nanofocusing of optical energy in tapered plasmonic waveguides. *Physical Review Letters*, 93(13):137404–1–137404–4, 2004. 1

[12] Andrews S.R.-Marten-Moreno L. Garca-Vidal F.J. Maier, S.A. Terahertz surface plasmon-polariton propagation and focusing on periodically corrugated metal wires. *Physical Review Letters*, 97(17), 2006. 1

[13] Podolskiy V.A. Govyadinov, A.A. Metamaterial photonic funnels for subdiffraction light compression and propagation. *Physical Review B - Condensed Matter and Materials Physics*, 73(15):1–5, 2006. 1

[14] Alu A.-Silveirinha-M.G. Engheta N. Edwards, B. Reflectionless sharp bends and corners in waveguides using epsilon-near-zero effects. *Journal of Applied Physics*, 105(4), 2009. cited By (since 1996) 0. 1, 12, 32

[15] Lopetegi T.-Laso-M.A.G. Baena J.D.-Bonache J. Beruete M. Marques R. Martn F. Sorolla M. Falcone, F. Babinet principle applied to the design of metasurfaces and metamaterials. *Physical Review Letters*, 93(19):197401–1–197401–4, 2004. cited By (since 1996) 105. 11

[16] W. Rotman. Plasma simulation by artificial dielectrics and parallel-plate media. *IRE Trans. Antennas Propag.*, 10(1):82–95, 1962. 12

[17] Martel J.-Mesa-F. Medina F. Marques, R. Left-handed-media simulation and transmission of em waves in subwavelength split-ring-resonator-loaded metallic waveguides. *Physical Review Letters*, 89(18):183901/1–183901/4, 2002. 12

[18] Jelinek L.-Marques-R. Medina F. Baena, J.D. Near-perfect tunneling and amplification of evanescent electromagnetic waves in a waveguide filled by a metamaterial: Theory and experiments. *Physical Review B - Condensed Matter and Materials Physics*, 72(7), 2005. 12

[19] R. E. Collin. *Field Theory of Guided Waves*. John Wiley and Sons, 1991. pp.471-483. 19, 20, 21

[20] Engheta N. Alu, A. Dielectric sensing in -near-zero narrow waveguide channels. *Physical Review B - Condensed Matter and Materials Physics*, 78(4), 2008. 36